

Evaluation of cloud-resolving model intercomparison simulations using TWP-ICE observations: Precipitation and cloud structure

Adam Varble,¹ Ann M. Fridlind,² Edward J. Zipser,¹ Andrew S. Ackerman,² Jean-Pierre Chaboureau,³ Jiwen Fan,⁴ Adrian Hill,⁵ Sally A. McFarlane,⁴ Jean-Pierre Pinty,³ and Ben Shipway⁵

Received 11 October 2010; revised 1 February 2011; accepted 21 March 2011; published 24 June 2011.

[1] The Tropical Warm Pool–International Cloud Experiment (TWP-ICE) provided extensive observational data sets designed to initialize, force, and constrain atmospheric model simulations. In this first of a two-part study, precipitation and cloud structures within nine cloud-resolving model simulations are compared with scanning radar reflectivity and satellite infrared brightness temperature observations during an active monsoon period from 19 to 25 January 2006. Seven of nine simulations overestimate convective area by 20% or more leading to general overestimation of convective rainfall. This is balanced by underestimation of stratiform rainfall by 5% to 50% despite overestimation of stratiform area by up to 65% because of a preponderance of very low stratiform rain rates in all simulations. All simulations fail to reproduce observed radar reflectivity distributions above the melting level in convective regions and throughout the troposphere in stratiform regions. Observed precipitation-sized ice reaches higher altitudes than simulated precipitation-sized ice despite some simulations that predict lower than observed top-of-atmosphere infrared brightness temperatures. For the simulations that overestimate radar reflectivity aloft, graupel is the cause with one-moment microphysics schemes whereas snow is the cause with two-moment microphysics schemes. Differences in simulated radar reflectivity are more highly correlated with differences in mass mean melted diameter (D_m) than differences in ice water content. D_m is largely dependent on the mass-dimension relationship and gamma size distribution parameters such as size intercept (N_0) and shape parameter (μ). Having variable density, variable N_0 , or μ greater than zero produces radar reflectivities closest to those observed.

Citation: Varble, A., A. M. Fridlind, E. J. Zipser, A. S. Ackerman, J.-P. Chaboureau, J. Fan, A. Hill, S. A. McFarlane, J.-P. Pinty, and B. Shipway (2011), Evaluation of cloud-resolving model intercomparison simulations using TWP-ICE observations: Precipitation and cloud structure, *J. Geophys. Res.*, 116, D12206, doi:10.1029/2010JD015180.

1. Introduction

[2] Realistic modeling of tropical convection and its climatic effects across a wide range of domain scales is a foremost objective in current atmospheric research. Cloud-resolving models (CRMs) are critical to this objective as they provide a wealth of information on in-cloud processes that cannot be directly measured and are therefore central to improving parameterizations within larger scale operational

and general circulation models (GCMs). For CRM output to be wholly utilized, it should be able to realistically reproduce statistical distributions of available observations. This requires accurately simulating convective and mesoscale precipitation processes. The Tropical Warm Pool–International Cloud Experiment (TWP-ICE) [May *et al.*, 2008], conducted in and around Darwin, Australia in January and February of 2006, produced high quality model forcing and observational data sets. Using these data, an objective of TWP-ICE was to allow comparisons of model simulations with observations for the purpose of improving model representations of tropical convection.

[3] During the monsoonal wet season, Darwin experiences active and break periods generally characterized by westerly oceanic and easterly continental winds, respectively. Active period convective systems typically exhibit tropical oceanic characteristics, whereas the break period systems exhibit more continental characteristics [Keenan and Carbone, 1992; May *et al.*, 2008]. The TWP-ICE campaign was characterized by active conditions from January 19 through January 25

¹Department of Atmospheric Sciences, University of Utah, Salt Lake City, Utah, USA.

²NASA Goddard Institute for Space Studies, New York, New York, USA.

³Laboratoire d’Aérologie, University of Toulouse/CNRS, Toulouse, France.

⁴Department of Climate Physics, Pacific Northwest National Laboratory, Richland, Washington, USA.

⁵Met Office, Exeter, UK.

followed by an unusual suppressed westerly period through February 2, a clear period through February 5, and then break conditions for the rest of the experiment [May *et al.*, 2008]. The active monsoon is the focus of this study as this is the regime closest to the tropical oceanic convective regime that covers a large area of the tropics [Jakob and Tselioudis, 2003; May *et al.*, 2008].

[4] Past tropical convection studies have focused on comparing observations such as radar and satellite data to model simulation output. Such studies have also focused on field campaigns such as the Tropical Rainfall Measuring Mission Large-Scale Biosphere–Atmosphere (TRMM LBA) [Lang *et al.*, 2007], the Kwajalein Experiment (KWAJEX) [Blossey *et al.*, 2007; Li *et al.*, 2008; Matsui *et al.*, 2009], and the South China Sea Monsoon Experiment (SCSMEX) [Matsui *et al.*, 2009]. Most studies [Blossey *et al.*, 2007; Lang *et al.*, 2007; Li *et al.*, 2008; Matsui *et al.*, 2009] agree that simulated radar reflectivity in convective regions is too high while simulated microwave brightness temperatures are too low. This is generally attributed to one-moment microphysics schemes producing excessive amounts of graupel [Lang *et al.*, 2007; Li *et al.*, 2008; Matsui *et al.*, 2009] despite reasonable vertical velocities [Lang *et al.*, 2007; Li *et al.*, 2008] in convective regions. Less attention has been paid to stratiform regions, although Blossey *et al.* [2007] point out that unrealistically high convective precipitation efficiency likely negatively affects stratiform region properties in simulations.

[5] Whereas most of the foregoing studies have focused on multiple simulations and sensitivity tests with a single model [e.g., Blossey *et al.*, 2007], model intercomparison studies tend to focus on a small number of simulations performed by many different models with different schemes. Quite a few such model intercomparison studies have now been performed through the Global Energy and Water-Cycle Experiment (GEWEX) Cloud Systems Study (GCSS) program described by Randall *et al.* [2003]. These include single column model (SCM) and CRM intercomparison studies for the Tropical Oceans Global Atmosphere Coupled Ocean–Atmosphere Research Experiment (TOGA-COARE) [Moncrieff *et al.*, 1997; Redelsperger *et al.*, 2000; Bechtold *et al.*, 2000], multiple studies over the Atmospheric Radiation Measurement (ARM) Climate Research Facility (ACRF) Southern Great Plains (SGP) site [Ghan *et al.*, 2000; Xu *et al.*, 2002; Xie *et al.*, 2002, 2005], and studies over tropical land [Grabowski *et al.*, 2006; Petch *et al.*, 2007; Willett *et al.*, 2008]. Although there have been specific focus areas in each of these studies, they share a common goal of improving climate prediction. Since SCMs and CRMs are valuable tools in guiding representation of tropical convection and its effects in GCMs, climate modeling skill is improved when SCMs and CRMs provide more realistic output.

[6] The TWP-ICE CRM intercomparison study [Fridlind *et al.*, 2010] adds to this list of model intercomparison studies and is one of four such TWP-ICE studies; the others use SCMs, limited-area models (LAMs, with open boundary conditions and nested domains), and GCMs run in operational forecasting mode. As with previous studies, the TWP-ICE intercomparison focuses on comparing domain wide observed and simulated properties such as precipitation rate, thermodynamic processes, and the radiation budget (A. M. Fridlind *et al.*, manuscript in preparation, 2011). Several

studies have already used TWP-ICE data to evaluate various SCM, CRM, and LAM simulations. Foci have included updraft properties and entrainment rates [Wang and Liu, 2009; Wu *et al.*, 2009; Zhang, 2009; Del Genio and Wu, 2010], ice microphysics [Wang *et al.*, 2009], and precipitation rates [Wapler *et al.*, 2010].

[7] The focus of part 1 of this study is establishing differences between simulated and observed precipitation and cloud top structures. For precipitation, this analysis is performed separately on convective and stratiform regions. Dynamics are profoundly different in each region [Houze, 1997], associated with distinct differences in the microphysical growth processes [Houghton, 1968; Houze, 1997] and vertical distribution of diabatic heating [Houze, 1982, 1989, 1997; Johnson, 1984] in each region. Part II of this study compares additional simulated and observed dynamical and microphysical properties with the goal of explaining structural differences established within part I. Whereas part I focuses on convective and stratiform regions independently, part II will also examine the connection between them. It is well established that stratiform regions in the tropics would not exist without ice advection from convective regions [Smull and Houze, 1985; Rutledge and Houze, 1987; Biggerstaff and Houze, 1991]. Therefore, model biases in convective properties can easily lead to model biases in stratiform regions.

[8] While bin microphysics schemes have become more commonplace for research applications, bulk schemes remain the workhorse for most applications because their greater computational efficiency allows simulations on larger spatial scales and longer time scales. In this study, nine different simulations from four different models employing bulk schemes of varying complexity are compared with observations using 3-hourly observations and output from the simulations. By virtue of the use of several different dynamics and microphysics schemes, a wide range of results is to be expected, with differences between models and observations dependent on the diagnostic being compared. Exploring causes for these differences provides a pathway to improving CRM parameterizations and the veracity of output used for GCM parameterization development. It is widely known that GCMs are hindered by inadequate representation of tropical cloud systems, their thermodynamic and radiative impacts, and their relationship to environmental properties [Del Genio and Kovari, 2002; Neale and Slingo, 2003; Stephens, 2005; Randall *et al.*, 2007]. Consequently, it is pertinent to determine if CRM representation of tropical convective systems is accurate. The remaining portion of the paper is separated into five sections. Model simulations are described in section 2 and observations in section 3. Results are presented in section 4 with discussion in section 5, and conclusions in section 6.

2. Models

[9] The configurations of the nine model simulations (all 3D) are given in Table 1. The four dynamics models used are the Distributed Hydrodynamic-Aerosol-Radiation Model Application (DHARMA) [Stevens *et al.*, 2002; Ackerman *et al.*, 2000], the UK Met Office Large Eddy Model (UKMO) [Shutts and Gray, 1994; Petch and Gray, 2001], the Meso-NH Atmospheric Simulation System (MESONH) [Lafore *et al.*, 1998], and the System for Atmospheric Modeling (SAM)

Table 1. The Configurations of the Nine Model Simulations Including the Symbols Used in the Figures^a

Simulation	Symbol	Model Simulation Configurations			
		Domain	Δx	Δz	Microphysics
DHARMA-B	Solid diamond	(176 km) ²	917 m	100–250 m	one-moment
DHARMA-S	Open diamond	(176 km) ²	917 m	100–250 m	one-moment
UKMO-1	Right-pointing triangle	(177 km) ²	917 m	225–500 m	two-moment (i)
UKMO-2	Left-pointing triangle	(177 km) ²	917 m	225–500 m	two-moment (i, g, s)
UKMO-2M	Square	(177 km) ²	917 m	225–500 m	two-moment (i, r, g, s)
MESONH-1	Up-pointing triangle	(192 km) ²	1000 m	100–250 m	one-moment
MESONH-2	Down-pointing triangle	(192 km) ²	1000 m	100–250 m	two-moment (i, w)
SAM-B	Solid circle	(192 km) ²	1000 m	100–400 m	two-moment (i, w, r, g, s)
SAM-S	Open circle	(192 km) ²	1000 m	100–400 m	two-moment (i, w, r, g, s)

^aBaseline simulations are represented by filled symbols and sensitivity simulations are represented by open symbols. If a simulation has two-moment species, then they are indicated in parentheses: I, cloud ice; w, cloud water; r, rain; g, graupel; and s, snow.

[Khairoutdinov and Randall, 2003]. Four of the nine simulations use one-moment microphysical schemes and the others use different forms of two-moment schemes. If the number concentration of a hydrometeor species is predicted, it is shown by a letter in parentheses in the Microphysics column of Table 1. Two of the nine simulations are referred to as sensitivity runs (ending in ‘-S’) whereas the others are referred to as baseline runs. A sensitivity simulation uses 6 h nudging of domain-averaged potential temperature and water vapor at full strength above 1 km and at a strength that linearly decreases to zero at 0.5 km, whereas a baseline simulation is nudged at full strength only above 16 km and at a strength that linearly decreases to zero at 15 km. By nudging the mean profile to observations, deviations from the mean are preserved. The sensitivity simulations give an idea of accumulating error associated with long-term application of the forcing.

[10] Two DHARMA simulations, one baseline (DHARMA-B) and one sensitivity (DHARMA-S), use a one-moment scheme that predicts the mass mixing ratios of four species: cloud water, rain, graupel, and a mixed category of cloud ice and snow [Grabowski, 1999]. Three UKMO baseline simulations include a one-moment run (UKMO-1) and two different two-moment runs (UKMO-2, UKMO-2M). All simulations predict the mass mixing ratios of cloud water, rain, graupel, snow, and cloud ice. UKMO-1 additionally predicts the number concentration of cloud ice; however a separate diagnostic concentration derived from Meyers *et al.* [1992] is used for calculations in this study. UKMO-2 also predicts the number concentrations of snow and graupel, and UKMO-2M predicts the number concentrations of cloud ice, snow, graupel, and rain using the scheme of Morrison *et al.* [2009] modified to use fixed cloud water concentration. The one-moment MESONH simulation (MESONH-1) predicts the mass mixing ratios of cloud water, rain, graupel, snow, and cloud ice [Pinty and Jabouille, 1998], while the two-moment simulation (MESONH-2) additionally predicts the number concentrations of cloud ice and cloud water [Pinty, 2002]. Last, there is one baseline (SAM-B) and one sensitivity (SAM-S) SAM simulation, both of which incorporate two-moment microphysics and predict the mass mixing ratio and number concentration of cloud water, rain, cloud ice, graupel, and snow [Morrison *et al.*, 2009]. Each simulation is represented by its own symbol in figures, with sensitivity simulations having open symbols and baseline simulations having filled symbols (see Table 1).

[11] Table 2 shows the advection, turbulence, surface flux, and radiation schemes used for each model. All models solve the anelastic equations and use advection schemes shown in the ‘Advection’ column of Table 2. Turbulence schemes use either a Smagorinsky-Lilly model [Lilly, 1967; Deardorff, 1970], a 1.5-order closure [Cuxart *et al.*, 2000], or an option of the two. Surface flux schemes for DHARMA and UKMO are based off of Monin-Obukhov similarity theory [Monin and Obukhov, 1954], whereas MESONH uses bulk iterative Exchange Coefficients from Unified Multi-Campaigns Estimates (ECUME) [Weill *et al.*, 2003; Belamari, 2005] and SAM uses the scheme in the National Center for Atmospheric Research Community Climate Model version 3.5 [Collins *et al.*, 1997]. Radiation schemes use fast radiative transfer calculations by the methods shown in the Radiation column of Table 2.

[12] The model specification is described in detail by Fridlind *et al.* [2010]. All simulations are run for 16 days starting at 0000 UT 18 January 2006 with 36 h allowed for spin-up. The pentagonal forcing domain defined by the radiosonde launch locations during TWP-ICE, shown in Figure 1, is approximately equivalent to a 176 km by 176 km square domain. As shown in Table 1, a few simulations have larger domains, and where necessary, statistics from these runs are normalized. Large-scale forcing for the models is 3 h domain-mean profiles defined using a constrained variational objective analysis on observational data, as described by Xie *et al.* [2010]. This forcing is applied continuously at full strength below 15 km and at a strength that linearly decreases to zero at 16 km because the profiles are poorly constrained by observations at higher altitudes [Fridlind *et al.*, 2010]. Mean horizontal winds are nudged to the observed mean continuously with a 2 h time scale. The model horizontal resolution is approximately 917 m for the DHARMA and UKMO simulations and 1000 m for all other simulations. Vertical resolution varies significantly between different simulations with spacing as fine as 100 m and as coarse as 500 m with as many as 102 levels (MESONH) and as few as 50 levels (UKMO). All simulations have periodic lateral boundary conditions and an oceanic lower boundary with a constant sea surface temperature of 29°C. The lower boundary includes a surface albedo that is fixed at 0.07, interactive surface fluxes, and interactive diurnal radiation.

[13] Several variables such as radar reflectivity and 10.8 μm satellite infrared (IR) brightness temperature (T_b) are calculated from model output for comparison with observed

Table 2. Advection, Turbulence, Surface Flux, and Radiation Schemes Used in the Four Models^a

Model	Model Schemes			
	Advection	Turbulence	Surface Flux	Radiation
DHARMA	Second-order forward in time with third-order upwinding advection [Stevens and Bretherton, 1996]	Smagorinsky-Lilly	Monin-Obukhov similarity theory	Two-stream with equivalent spheres [Toon et al., 1989]
MESONH	Fourth-order forward in time with piecewise parabolic method advection [Colella and Woodward, 1984]	1.5-order closure [Cuxart et al., 2000]	Bulk iterative Exchange Coefficients from Unified MultiCampaigns Estimates (ECUME) [Belamari, 2005]	Rapid Radiative Transfer Model [Mlawer et al., 1997] as used in the European Centre for Medium-Range Weather Forecasting [Gregory et al., 2000]
UKMO	Leapfrog scheme with a Robert-Asselin time filter; momentum advection is by Piacsek and Williams [1970]; Monotonic scalar advection is by Leonard et al. [1993]	Smagorinsky-Lilly	Monin-Obukhov similarity theory	Edwards-Slingo [Edwards and Slingo, 1996]
SAM	Third-order Adams-Basforth with variable time stepping, second-order momentum advection and monotonic positive-definite scalar advection [Smolarkiewicz and Grabowski, 1990]	Smagorinsky-type or 1.5-order closure dependent on the turbulent kinetic energy	NCAR Community Climate Model version 3.5 [Collins et al., 1997]	NCAR Community Climate Model (CCM3) [Kiehl et al., 1998]

^aAll models solve the equations of motion using the anelastic approximation.

variables. Observations from a 5.5 cm C band radar are used in this study, which puts precipitation-sized particles for oceanic tropical convection in the Rayleigh scattering regime. Therefore, simulated radar reflectivity is calculated by integrating the sixth moment of the hydrometeor melted equivalent diameter size distributions. For cloud ice, snow, and graupel, a dielectric factor of 0.208/0.93 is used [Smith, 1984]. Model rain rates are calculated at 2.5 km altitude by multiplying rain water content by the mass-weighted mean terminal fall speed. Volumetric rainfall is then computed by accumulating the rain rates over the domain at a given time step.

[14] Satellite radiances are simulated with the Joint Center for Satellite Data Assimilation (JCSDA) Community Radiative Transfer Model (CRTM) [Weng et al., 2005; Han et al., 2006] which takes profiles of temperature, water vapor, hydrometeor effective radii, and hydrometeor water contents as inputs. Other atmospheric constituents are defined with a built in climatological tropical atmosphere and a sea surface with constant temperature of 29°C is used. The CRTM simulates IR and microwave brightness temperatures for specific satellite sensors, including the 10.8 μm IR channel of the Multifunctional Transport Satellite (MTSAT). This radiative transfer model assumes a plane parallel atmosphere and uses Mie lookup tables for hydrometeor scattering. The radiative transfer equation is solved using advanced doubling and adding [Liu and Weng, 2006]. Based on the location of Darwin with respect to the geostationary satellite, a zenith angle of 17.8° is used for all model grid points.

[15] Chen et al. [2008] showed that model error was primarily attributed to uncertainty in observational input to the CRTM, cloud inhomogeneity, and assumed ice crystal habit. Clear sky bias was only 0.1 K and error attributable

to radiative transfer solver assumptions is very small. Our study does not have errors associated with input and cloud inhomogeneity because CRM output, not observations, is used as input to the CRTM. This leaves uncertainty resulting from assumed ice crystal habit. Huang et al. [2004] compared infrared T_b differences between assumed hexagonal ice crystals and assumed spherical ice crystals. The largest differences of ~2 K were found for small particle sizes ($10 \mu\text{m}$)

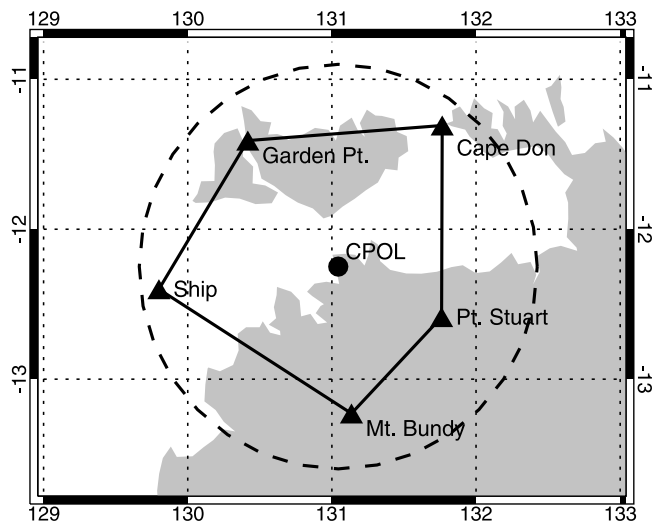


Figure 1. The five sites shown with triangles define the TWP-ICE pentagonal domain. Each site took 3-hourly soundings. The location of the CPOL radar used for observed radar reflectivity is also shown on the map as a black circle. The 150 km CPOL range ring is shown with a dashed line.

and low optical depths (0.5). The vast majority of CRM columns have larger optical thicknesses and effective sizes than 0.5 and 14 μm , respectively, and because of the large sample size, simulated IR T_b errors should be within ± 2 K.

[16] Additional error may be introduced into MESONH simulated brightness temperatures due to inconsistencies between CRM assumed snow properties and CRTM assumed snow properties. The CRTM assumes generalized gamma distributions with constant bulk densities for each hydrometeor species. The density of snow in MESONH varies greatly with size. At diameters less than 200 μm , the density of snow in MESONH is about 900 kg/m^3 , the same as cloud ice, whereas the CRTM assumes 100 kg/m^3 . For this reason, MESONH snow water contents and effective radii are included in the cloud ice input to the CRTM to minimize error.

3. Observations

[17] A central source of observational data is the C band polarimetric scanning radar (CPOL) described in detail by Keenan et al. [1998] and located at Gunn Point about 30 km northeast of Darwin. CPOL provides three-dimensional radar reflectivity at 10 min resolution. The radar reflectivity is interpolated onto a 2.5 km horizontal and 0.5 km vertical grid. Reflectivity uncertainty is estimated to be 1 dBZ (P. May, personal communication, 2010). Rain rates are calculated using a Z-R relationship for low rain rates, but make use of differential reflectivity (ZDR) and specific differential phase (KDP) for higher rain rates which brings down the uncertainty at higher rain rates. Uncertainty ranges from about 100% (e.g., 1 mm h^{-1} represents a range of 0.5 to 2 mm h^{-1}) for the lowest rain rates to 25% for rain rates of 10 mm h^{-1} or more (P. May, personal communication, 2010). The rain rates are calculated at a 2.5 km height due to radar beam height restrictions at far ranges, and these are the rain rates that went into the model forcing.

[18] Because the sensitivity of the CPOL radar is approximately 0 dBZ at a 150 km range and clutter was found to be an issue around 0 dBZ, comparisons with simulations are limited to reflectivities of 5 dBZ or greater. Hence, much of the nonprecipitating cloud information is not captured. The 10.8 μm channel on the MTSAT geostationary satellite provides complementary information on cloud structure revealed by smaller particles, such as those classified as cloud ice in the model microphysics schemes. Clouds interact with IR radiation at this wavelength far more effectively than the rest of the atmosphere, and for optically thick clouds, the 10.8 μm brightness temperature (T_b) gives an approximation of cloud top temperature. The effective resolution of the MTSAT pixel level data is about 5.17 km in the TWP-ICE domain. By comparing simulated top-of-atmosphere 10.8 μm brightness temperatures directly to observed top-of-atmosphere 10.8 μm brightness temperatures, multistep retrieval algorithms that introduce further errors are avoided.

4. Results

4.1. Approach

[19] Because the models in this study assume a lower oceanic boundary, only the active and suppressed periods were simulated. These are periods in which the air mass in place was more oceanic in nature than continental as it is

during the break period. All statistical results compare 3-hourly model output and observations for the 6 day active monsoon period spanning 12Z January 19 to 12Z January 25. For comparisons with both radar and satellite data, model output was degraded in horizontal resolution to 2.5 km and 5.17 km, respectively, while conserving radar reflectivity factor and IR T_b . In addition, because the models are forced by a finite pentagonal domain defined by five sounding stations, the observational data is limited to that domain for comparisons.

[20] Model output and observations are compared for convective and stratiform regions separately because of the fundamentally different radar reflectivity structure in each region [Houze, 1997] owing to distinctly different dynamical and microphysical processes. This allows radar reflectivity to be used as a separator of the two regions. The separation is performed using a texture algorithm on 2.5 km altitude horizontal radar reflectivity following Steiner et al. [1995]. Because CPOL sensitivity is limited to radar reflectivities greater than approximately 0 dBZ, all grid points in both models and observations that have a radar reflectivity less than 0 dBZ are set to 0 dBZ for the application of Steiner et al.'s [1995] algorithm. For comparisons between models and observations, only radar reflectivities greater than or equal to 5 dBZ are considered to filter out clutter. Every compared variable except for IR T_b is separated into convective and stratiform components.

4.2. Rainfall

[21] Table 3 shows that the models come very close to reproducing the observed mean total volumetric rainfall, not surprisingly since observed rainfall is an influential input to model forcing (see Xie et al. [2010]). All simulations except for MESONH-2 and SAM-S are within 10% of observations. This does not mean, however, that mean rain rates and precipitating area are close to observed. In fact, as shown in Tables 3 and 4, all baseline simulations underestimate mean rain rate by more than 15% and overestimate the precipitating area by 35% or greater. The sensitivity simulations are closer to observed precipitating area and mean rain rates. When rainfall is split into convective and stratiform components, several common patterns emerge.

4.2.1. Convective Regions

[22] Figure 2b shows that the time series of convective rainfall in most simulations follows observations closely. Table 3 shows that most model results are either close to or somewhat higher than the observed convective rainfall. UKMO-1, UKMO-2, MESONH-1, and SAM-S all produce convective rainfall within 10% of that observed. DHARMA-B, UKMO-2M and SAM-B overestimate convective rainfall by twice that, although still within observational uncertainty. There are two simulations beyond observational uncertainty. MESONH-2 underpredicts convective rainfall by 42% and DHARMA-S overpredicts it by 35%.

[23] Convective rainfall is equal to convective area multiplied by convective rain rate. Figure 2a shows that most simulations reproduce the temporal variability of convective area correctly but overestimate convective area during both the peak and decay of precipitation events. Mean convective area, expressed as a fraction of the domain, is shown in Table 4. Five simulations (DHARMA-B, DHARMA-S, UKMO-2M, MESONH-1, and SAM-B) overestimate mean

Table 3. The Mean Rainfall for All Precipitating Regions, Convective Regions, and Stratiform Regions^a

	Volumetric Rainfall					
	All		Convective		Stratiform	
	Mean	Difference (%)	Mean	Difference (%)	Mean	Difference (%)
Observed	33.36 (23.66–48.51)	-	20.68 (16.19–26.59)	-	12.68 (7.48–21.92)	-
DHARMA-B	35.66	+7	24.66	+19	11.00	-13
DHARMA-S	35.95	+8	27.90	+35	8.05	-37
UKMO-1	35.26	+6	23.20	+12	12.06	-5
UKMO-2	36.65	+10	24.79	+20	11.85	-7
UKMO-2M	34.92	+5	25.98	+26	8.93	-30
MESONH-1	33.11	-1	23.79	+15	9.33	-26
MESONH-2	20.52	-38	11.96	-42	8.55	-33
SAM-B	35.50	+6	26.12	+26	9.37	-26
SAM-S	27.41	-18	21.14	+2	6.27	-51

^aPrecipitation is defined as any radar reflectivity echoes greater than or equal to 5 dBZ at a height of 2.5 km. All precipitation is defined as either convective or stratiform following Steiner et al. [1995]. The percentage difference between each model simulation and observations is also shown. The mean rainfalls in parentheses show the lower and upper bounds with observational error taken into account. Rainfall has units of $10^3 \text{ mm h}^{-1} \text{ km}^2$.

convective area by more than 50%. Only two simulations (UKMO-1 and MESONH-2) are within 10% of observations. Table 5 shows that UKMO-1 and UKMO-2 produce mean convective rain rates within 10% of observed. DHARMA-B and DHARMA-S underestimate mean convective rain rate by 22% and 15%, respectively. The other simulations underestimate mean convective rain rate by 25% or less, with only MESONH-2 well beyond the range of observational uncertainty.

[24] The normalized cumulative distribution of rain rate is shown in Figure 3a with the rain rate cumulative contribution to convective rainfall in Figure 3b. The median (50th percentile) convective rain rate in observations is approximately 10 mm h^{-1} with a lower bound of 8.5 mm h^{-1} including observational uncertainty. The median ranges from about 5.5 mm hr^{-1} for a few simulations to 9.5 mm h^{-1} for UKMO-1 and UKMO-2. This excess of relatively small to moderate convective rain rates in all but the UKMO-1 and UKMO-2 simulations does not lead to underestimated convective rainfall because of high convective area. Figure 3b shows that these smaller rain rates contribute more to convective rainfall than in observations, but so do very high rain

Table 4. The Mean Domain Fraction Covered by Any Precipitation, Convective Precipitation, and Stratiform Precipitation^a

	Precipitating Area					
	All		Convective			
	Mean	Difference (%)	Mean	Difference (%)	Mean	Difference (%)
Observed	0.363	-	0.044	-	0.319	-
DHARMA-B	0.491	+35	0.068	+55	0.423	+33
DHARMA-S	0.379	+2	0.071	+61	0.308	-3
UKMO-1	0.507	+40	0.047	+7	0.460	+44
UKMO-2	0.496	+37	0.053	+20	0.443	+39
UKMO-2M	0.517	+42	0.073	+66	0.444	+39
MESONH-1	0.521	+44	0.068	+55	0.453	+42
MESONH-2	0.521	+44	0.042	-5	0.479	+50
SAM-B	0.598	+65	0.072	+64	0.526	+65
SAM-S	0.360	-1	0.057	+30	0.303	-5

^aPrecipitation is defined as any radar reflectivity echoes greater than or equal to 5 dBZ at a height of 2.5 km. All precipitation is defined as either convective or stratiform following Steiner et al. [1995]. The percentage difference between each model simulation and observations is also shown.

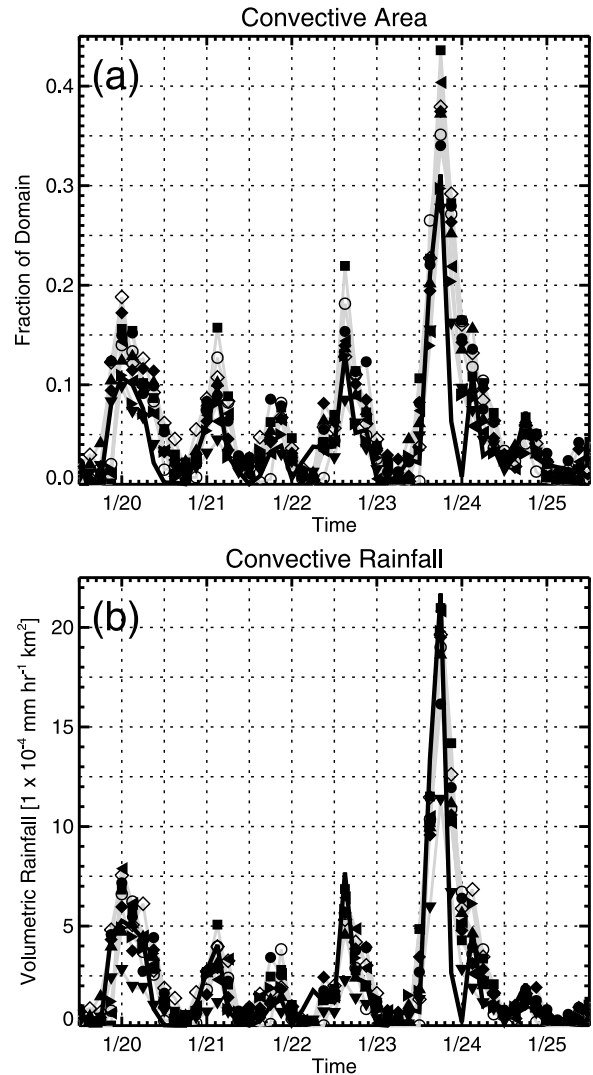


Figure 2. (a) The time series of convective area with model lines in gray and symbols (see Table 1). The thick black line represents observations derived from the CPOL radar. (b) The time series of convective volumetric rainfall at 2.5 km with units of $1 \times 10^{-4} \text{ mm h}^{-1} \text{ km}^{-2}$.

Table 5. The Mean Rain Rate for All Precipitating Regions, Convective Regions, and Stratiform Regions^a

	Rain Rate					
	All		Convective		Stratiform	
	Mean	Difference (%)	Mean	Difference (%)	Mean	Difference (%)
Observed	2.95 (2.09–4.29)	-	15.14 (11.85–19.47)	-	1.27 (0.75–2.20)	-
DHARMA-B	2.37	-20	11.86	-22	0.85	-33
DHARMA-S	3.10	+5	12.84	-15	0.85	-33
UKMO-1	2.25	-24	15.98	+6	0.85	-33
UKMO-2	2.39	-19	15.17	0	0.87	-31
UKMO-2M	2.19	-26	11.57	-24	0.65	-49
MESONH-1	2.10	-29	11.58	-24	0.68	-46
MESONH-2	1.30	-56	9.46	-38	0.59	-54
SAM-B	1.96	-34	11.99	-21	0.59	-54
SAM-S	2.51	-15	12.15	-20	0.68	-46

^aPrecipitation is defined as any radar reflectivity echoes greater than or equal to 5 dBZ at a height of 2.5 km. All precipitation is defined as either convective or stratiform following Steiner et al. [1995]. The percentage difference between each model simulation and observations is also shown. The mean rain rates in parentheses show the lower and upper bounds with observational error taken into account. Rain rate has units of mm h⁻¹.

rates. Therefore, a larger range of rain rates contributes significantly to overall convective rainfall in simulations than in observations.

4.2.2. Stratiform Regions

[25] In contrast to convective rainfall, all simulations underestimate stratiform rainfall as shown in Figure 4b and Table 3. Despite a reasonable representation of mesoscale precipitation event timing, the time series clearly shows every model underestimating the three largest peaks in stratiform rainfall. When accumulated, DHARMA-B, UKMO-1, and UKMO-2 are closest to the observed stratiform rainfall of 12.68×10^3 mm h⁻¹ km² and are also the only simulations within 15% of observations. All of the other simulations underestimate stratiform rainfall by over 25%, but of those, SAM-S is the only one technically beyond observational uncertainty.

[26] Despite the underestimation of stratiform rainfall, all baseline simulations overestimate mean stratiform area by 33% to 65%. This is pronounced in the time series in Figure 4a. Only the sensitivity simulations are close to the observed

mean domain fraction of 0.312, as shown in Table 4. The baseline simulations range from 0.423 (DHARMA-B) to 0.526 (SAM-B). Despite the overestimation of mean stratiform area, mean stratiform rain rates shown in Table 5 are far less than observed. Only DHARMA-B, DHARMA-S, UKMO-1, and UKMO-2 are within observational uncertainty, underestimating the mean stratiform rain rate by about 30–40%. All other simulations are about 50% or more below the observed mean stratiform rain rate.

[27] The normalized cumulative distribution for stratiform rain rates is shown in Figure 5a with the rain rate cumulative contribution to stratiform rainfall in Figure 5b. The median observed rain rate is 0.45 mm h⁻¹. At this percentile, models range from 0.15 mm h⁻¹ for SAM-B to 0.45 mm h⁻¹ for the DHARMA simulations. Figure 5b shows that these small rain rates do not contribute much to the observed stratiform rainfall. Half of observed stratiform rainfall comes from rain rates higher than 3.2 mm h⁻¹. For all simulations except for UKMO-1 and UKMO-2, 25% or less of stratiform rainfall comes from rain rates over 3.2 mm h⁻¹. At higher percentiles,

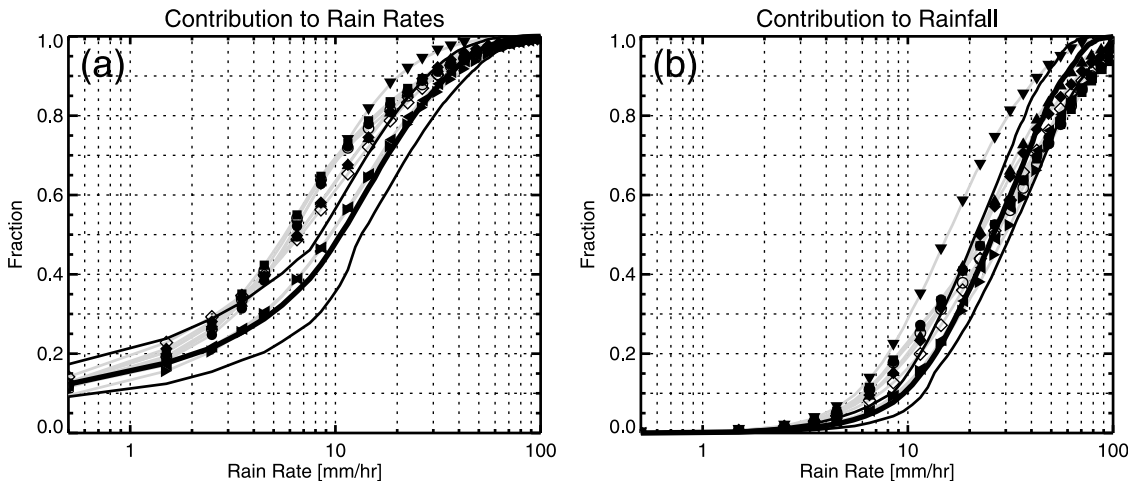


Figure 3. (a) The 2.5 km convective rain rate normalized cumulative distribution, with models represented by symbols (see Table 1) and observations represented by the thick black line. Thin black lines show the observational error bounds. (b) The cumulative contribution of convective rain rates to total convective rainfall. Observations are derived from the CPOL radar.

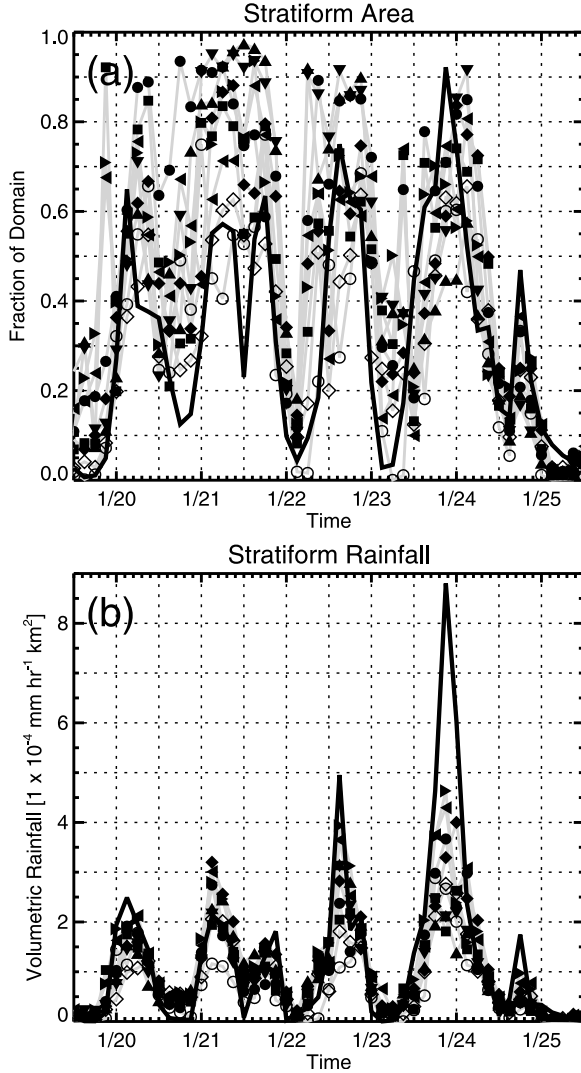


Figure 4. (a) The time series of stratiform area, with models represented by symbols (see Table 1). The thick black line represents observations derived from the CPOL radar. (b) The time series of stratiform volumetric rainfall at 2.5 km with units of $1 \times 10^{-4} \text{ mm h}^{-1} \text{ km}^{-2}$.

observed stratiform rain rates are much higher than all simulated rain rates as most simulations fall below the lower bound of observational uncertainty. Figures 4 and 5 together indicate that underestimation of stratiform rainfall is due to underestimation of stratiform rain rates rather than by underestimation of stratiform area.

4.3. Radar Reflectivity Structure

[28] As shown in Figures 2 and 4, the active monsoon period is characterized by several significant mesoscale rainfall events separated by periods of little rainfall. Representative horizontal plan views of the radar reflectivity field for a typical monsoonal precipitation event at 0300 UTC 20 January 2006 are shown in Figures 6 and 7 at altitudes of 2.5 and 7.5 km, respectively, representing levels respectively dominated by rain and ice. Structural differences between the different model simulations and observations are evident in the plan views.

[29] As will be shown in the comprehensive statistics that follow, there are systematic differences in simulated radar reflectivity and these are evident in the representative 2.5 km plan views. The three UKMO simulations have less small scale variability than the other simulations. The two SAM simulations have the broadest convective area with strong stratiform echoes, while the MESONH simulations produce less convective area than SAM with weaker trailing stratiform regions. Last, the DHARMA simulations produce more cellular convection embedded in weaker stratiform precipitation. Differences between baseline and sensitivity simulations are also noticeable as both sensitivity simulations produce noticeably higher convective radar reflectivity aloft and less stratiform area than their respective baseline simulations. Different microphysics schemes within the same model can produce very different results as well. For example, MESONH-2 has much less convective area relative to MESONH-1 and UKMO-2M produces a stratiform region with much higher radar reflectivity than the other two UKMO simulations.

[30] Systematic differences between models are also evident above the melting level at 7.5 km in Figure 7. MESONH is the only model with convective radar reflectivity low enough to be close to that observed. UKMO-2 is second closest to observations. All other simulations produce convective radar reflectivities aloft that are too high. Statistics clearly show that these differences are representative of the 6 day monsoon period in the next section. DHARMA-B, UKMO-1, and UKMO-2M produce small convective cores with high reflectivities, whereas DHARMA-S and the SAM simulations produce larger regions of high reflectivity. For stratiform regions, UKMO-2 is closest to observations. The other UKMO simulations and SAM simulations overestimate stratiform radar reflectivity. The SAM simulations produce the largest areas over 30 dBZ, something that is rare in observations at this level. The other two models, MESONH and DHARMA, do not produce extensive stratiform echoes that extend high enough. Differences evident in these snapshots are representative of differences throughout the active monsoon period, as discussed next.

4.3.1. Convective Regions

[31] To compare radar reflectivity for the entire 6 day active monsoon period, histograms at the 2.5 km and 7.5 km height levels are shown in Figures 8 and 9, respectively. These levels respectively represent the rain and ice regions as characteristic temperature for 2.5 km is approximately 13°C and for 7.5 km it is -13°C. All models reproduce the peak in samples between 35 and 40 dBZ at the 2.5 km height level seen in Figure 8, although all but two of the simulations (UKMO-1 and MESONH-2) have significantly higher peaks and wider distributions than observed. Simulations using the Morrison microphysics scheme (SAM-B, SAM-S, and UKMO-2M) also produce much higher peaks than the other model simulations. That the simulations reproduce the peaked distribution is not all that surprising because all of the microphysics schemes assume exponential distributions for rain. At 7.5 km (Figure 9a) the observed peak in samples drops to 20 dBZ, whereas the models fail to represent this distinct and almost symmetric peak. All simulations produce too many samples at reflectivities greater than 30 dBZ. The simulations employing two-moment schemes have more overall samples and more peaked distributions

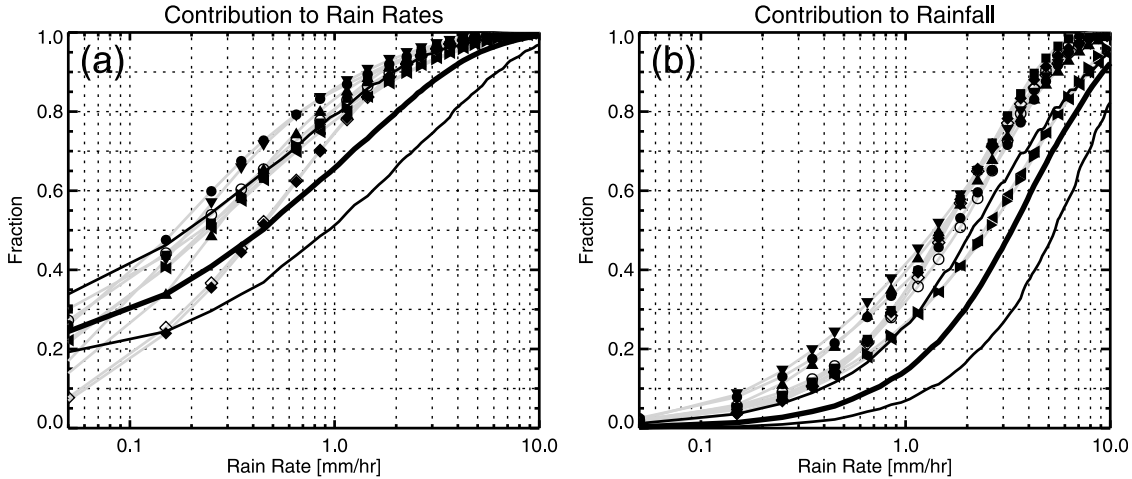


Figure 5. (a) The 2.5 km stratiform rain rate normalized cumulative distribution, with models represented by symbols (see Table 1) and observations represented by the thick black line. Thin black lines show the observational error bounds. (b) The cumulative contribution of stratiform rain rates to total stratiform rainfall. Observations are derived from the CPOL radar.

than the simulations employing one-moment schemes. This is due to differences in graupel and snow between the two scheme types. The simulated radar reflectivity due to graupel alone is shown in Figure 9b and due to snow alone in Figure 9c. Figures 9b and 9c clearly show that graupel is the primary cause of overestimation of radar reflectivity in the one-moment schemes. The distribution of radar reflectivity due to snow is decidedly more peaked. The positioning of the peak in snow radar reflectivity is different depending on the simulation. It is clear that snow causes the excessively high radar reflectivity in the three simulations that use the Morrison two-moment scheme.

[32] The vertical distribution of radar reflectivity is illustrated using normalized cumulative distributions of the maximum height of radar reflectivity thresholds. Figure 10a shows the maximum height of the 5 dBZ echo for all convective columns that have a 25 dBZ echo at or above the 5.5 km height level. It shows that the majority of model simulations do not produce enough deep convective regions. The shallowest convective cores are found in the MESONH-2 simulation and the deepest in the SAM-S simulation. The SAM-B simulation is unique in that close to 60% of 5 dBZ echo tops are found between 8 and 10 km. The rest of the simulations are closer to observations, but are offset to slightly lower echo tops. When the echo top threshold is increased to 25 dBZ (Figure 10b), observations have the lowest echo tops. The simulations closest to observations are MESONH-2 and SAM-B, although the 5 dBZ echo tops of these simulations are far lower than observed. An outlier in the other direction is the SAM-S simulation, with 25 dBZ echo tops up to 7 km higher than observations at some percentiles. Subtracting the height of the 25 dBZ echo top from the 5 dBZ echo top yields the cumulative distribution in Figure 10c. This panel shows that, on average, the convective radar reflectivity decreases with height more quickly near storm top in simulations than in observations. The median difference between the 25 dBZ and 5 dBZ echo top is 6 km in observations but only 1–3 km in simulations. This offset exists at all percentiles of the cumulative

distribution showing that there are clear differences in the vertical distribution of hydrometeor properties in observations and models.

4.3.2. Stratiform Regions

[33] Compared with the convective regions, there is much more spread between models and observations below the melting level in stratiform regions. At 2.5 km (Figure 11) observed radar reflectivity samples remain fairly constant between 5 and 30 dBZ and quickly diminish to nothing by 40 dBZ. The model simulations have more peaked distributions with peaks anywhere from 10 to 20 dBZ. The baseline simulations also have significantly more samples than the observations consistent with the general overestimation of stratiform area in those simulations. The UKMO-2M simulation is unique with many more samples at high reflectivities and a lower flatter peak than other simulations in better agreement with observations. This is interesting because UKMO-2M does not have the most stratiform rainfall or highest stratiform rain rates. The sensitivity simulations greatly reduce the number of samples and amplitude of peaks relative to their respective baseline simulations, suggesting that the overly high peaks at low reflectivities and overly large stratiform area could be related to the prescribed model forcing. That the simulations perform worse in stratiform rain than convective rain may be due to the exponential distribution not being representative of most stratiform rain. At 7.5 km (Figure 12a) the simulations exhibit a diverse spread in distributions with none particularly close to the observed distribution, which maintains a similar distribution to 2.5 km but shifted approximately 10 dBZ toward lower values. In contrast to observations, most simulations still maintain peaks between 5 and 15 dBZ and have gently decaying distributions with increasing reflectivity. The overall number of samples, however, greatly varies between simulations. The MESONH and DHARMA simulations significantly underestimate the overall number of samples, whereas the baseline Morrison microphysics runs (SAM-B and UKMO-2M) greatly overestimate the overall number of samples. It is clear from these plots that

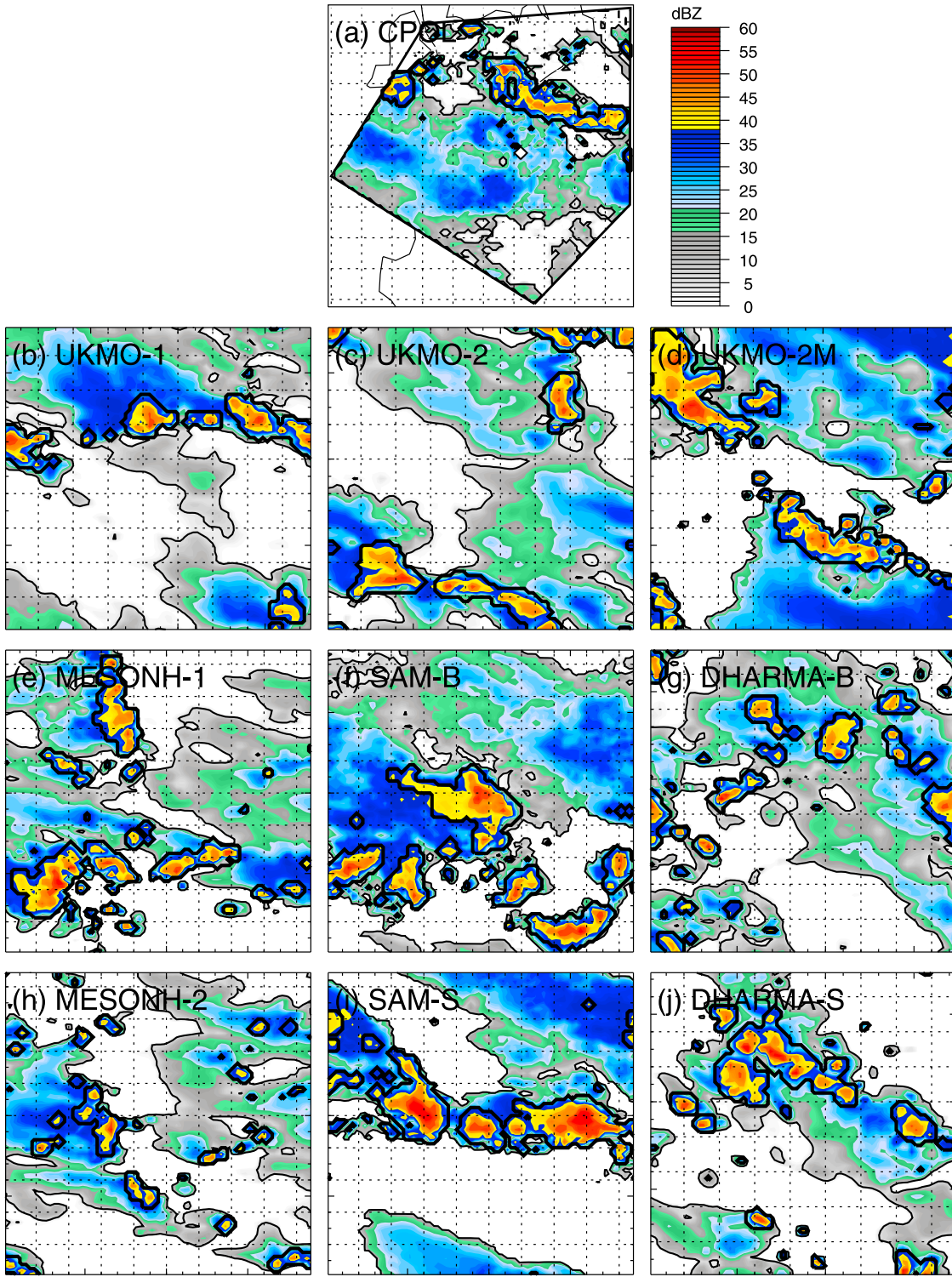


Figure 6. Representative 2.5 km horizontal cross sections of radar reflectivity at 0300 UTC 20 January 2006: (a) CPOL, (b) UKMO-1, (c) UKMO-2, (d) UKMO-2M, (e) MESONH-1, (f) SAM-B, (g) DHARMA-B, (h) MESONH-2, (i) SAM-S, and (j) DHARMA-S. Convective regions are outlined in thick black and stratiform regions in thin black.

while model simulations are different from each other, none resemble the observed distributions of stratiform reflectivity aloft. As shown in Figures 12b and 12c, these distributions are essentially distributions of snow radar reflectivity as

precipitation sized graupel is much more scarce in stratiform regions. That there is any significant graupel at all is very likely due to both the lack of a defined transition zone between convective and stratiform regions and the limitation

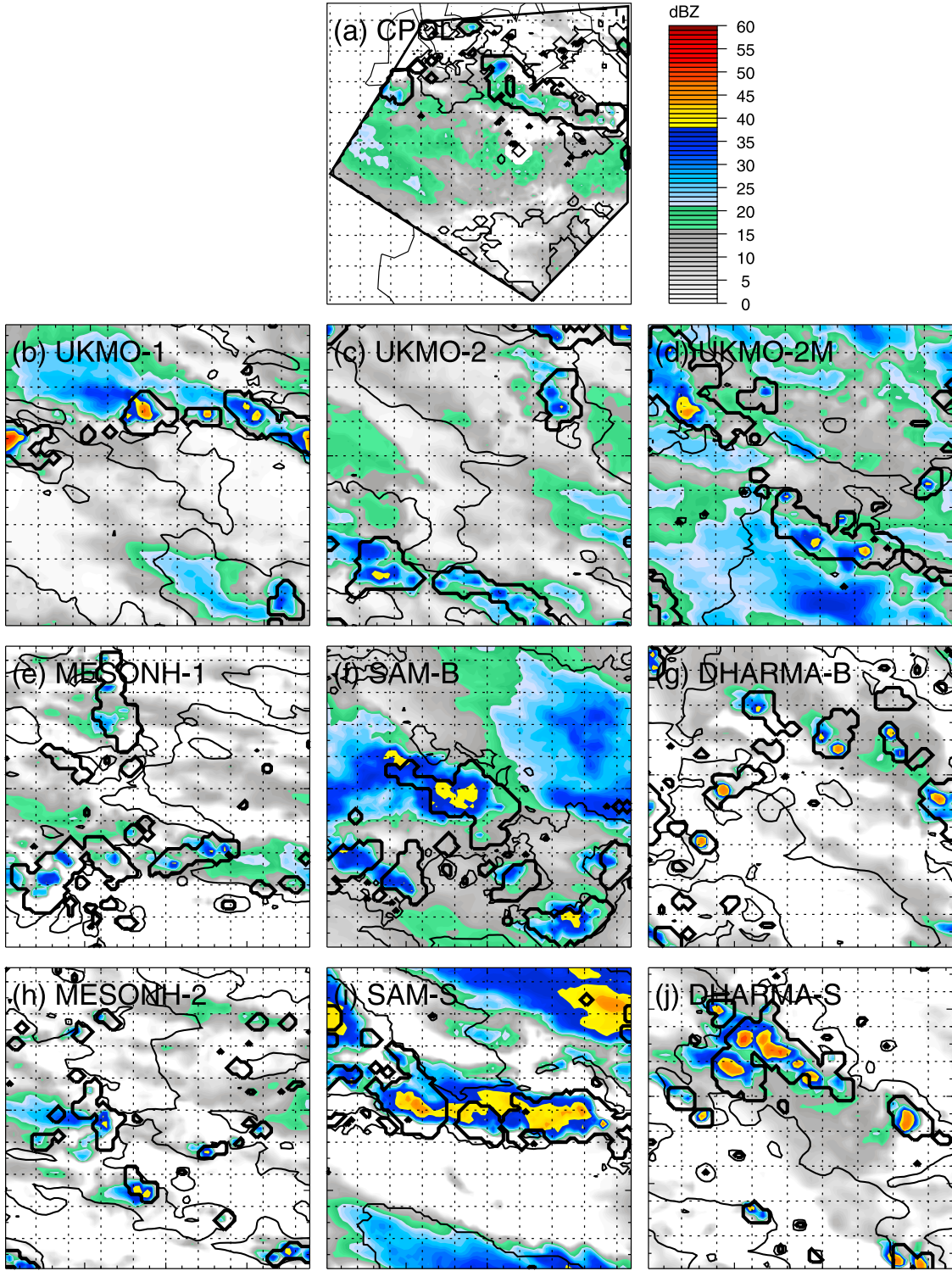


Figure 7. Representative 7.5 km horizontal cross sections of radar reflectivity at 0300 UTC 20 January 2006: (a) CPOL, (b) UKMO-1, (c) UKMO-2, (d) UKMO-2M, (e) MESONH-1, (f) SAM-B, (g) DHARMA-B, (h) MESONH-2, (i) SAM-S, and (j) DHARMA-S. Convective regions are outlined in thick black and stratiform regions in thin black.

of only two hydrometeor categories for precipitation sized ice.

[34] As in convective regions, Figure 13a shows that all model simulations have shallower stratiform 5 dBZ echo

tops than observations when the distribution is normalized. Only stratiform columns that have at least a 20 dBZ echo present at 5.5 km or above are included to focus on well-developed stratiform regions and remove possible bright

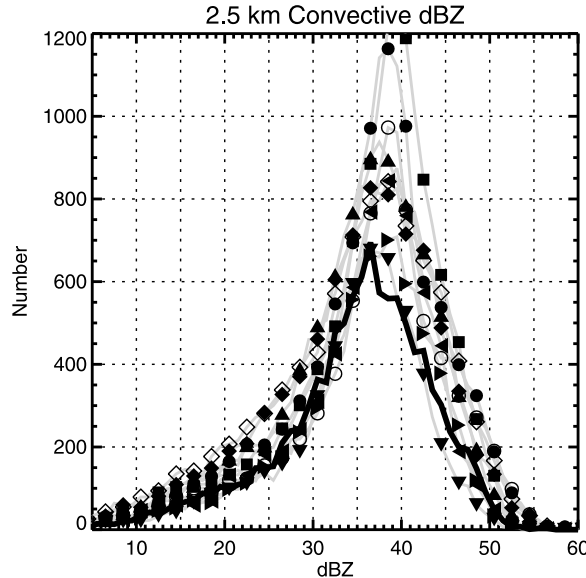


Figure 8. Histogram of observed and simulated convective radar reflectivity at 2.5 km. Models are represented by symbols (see Table 1), and the thick black line represents observations from the CPOL radar.

band effects in observations. About half of observed 5 dBZ echo tops are greater than 12 km. Most simulations are offset to lower heights by about 1–2 km. The order of these simulations is very similar to the convective regions and the uniform SAM-B echo tops seen in the convective echoes are present in stratiform echoes as well with 80% of 5 dBZ echo tops between approximately 7 and 10 km. A major shift occurs when increasing the echo top threshold to 20 dBZ, also as in the convective regions. Observed 20 dBZ echo tops are lower at all percentiles than in simulations with very few observed 20 dBZ echo tops above 9 km. Simulations, however, produce between 5% and 25% of 20 dBZ echo tops above 8 km. Figure 13c shows that when the height of the 20 dBZ echo top is subtracted from the height of the 5 dBZ echo top, the difference is much larger at all percentiles in observations. The offset between models and observations is anywhere from 1.5 to 4 km depending on the percentile and model. Because of the similarities between convective and stratiform regions, it is clear that disparities between these two regions are related, but it is unclear the degree to which these problems can be attributed to dynamics rather than microphysics.

4.4. Top-of-Atmosphere 10.8 μm Brightness Temperature

[35] As was shown in the last two sections, despite total simulated volumetric rainfall being fairly close to observations, radar reflectivities in mixed-phase and ice regions aloft are generally substantially different from observations. Hence, cloud top heights and cloud coverage are also likely to be substantially different. For optically thick clouds, such as precipitating clouds, the 10.8 μm top-of-atmosphere T_b is a useful proxy for cloud top height as discussed earlier.

[36] Representative plots of IR T_b at 0300 UT 20 January are shown in Figure 14 for each model simulation and for MTSAT measurements. Four of the nine model simulations

(MESONH-1, MESONH-2, SAM-B, and UKMO-2M) produce more persistent cold brightness temperatures that are less variable than those observed. Of these, the coldest brightness temperatures are produced by MESONH-2. Other simulations produce variability in T_b not unlike that observed. Specifically, UKMO-1, UKMO-2, and the DHARMA simulations produce spatial variability most resembling the observations.

[37] The cumulative distribution of brightness temperatures for the whole 6 day monsoon period shows a wide spread in Figure 15. The estimated error of ± 2 K primarily results from ice crystal habit assumptions, as mentioned earlier. The order of the model simulations with respect to

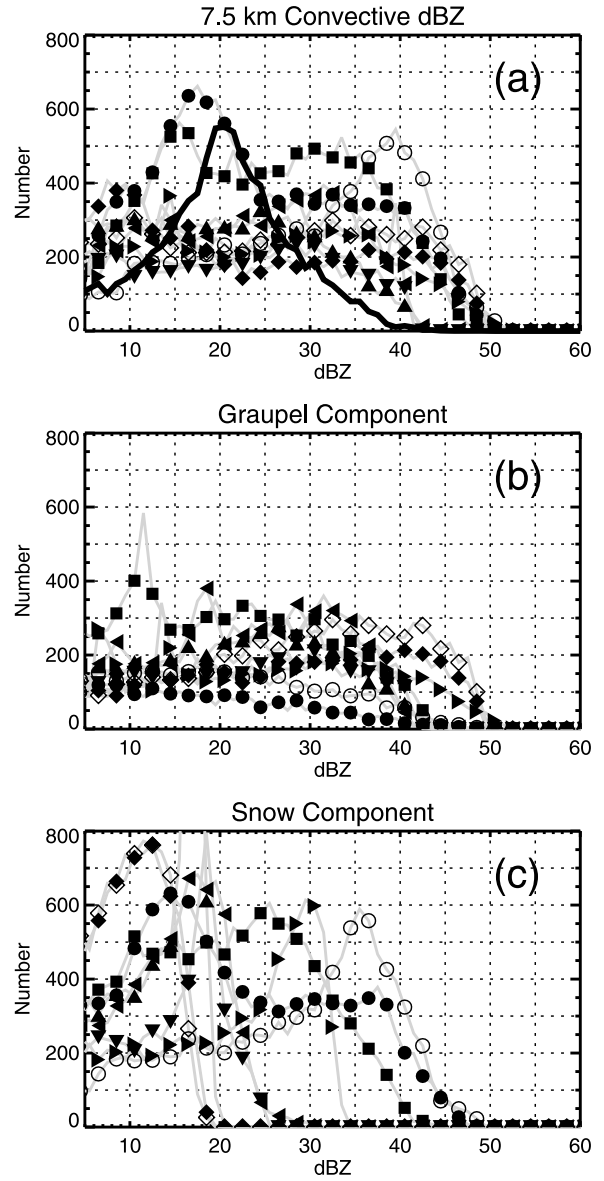


Figure 9. Histograms of (a) 7.5 km observed and simulated convective radar reflectivity, (b) 7.5 km simulated graupel radar reflectivity, and (c) 7.5 km simulated snow radar reflectivity. Models are represented by symbols (see Table 1), and the thick black lines represent observations from the CPOL radar.

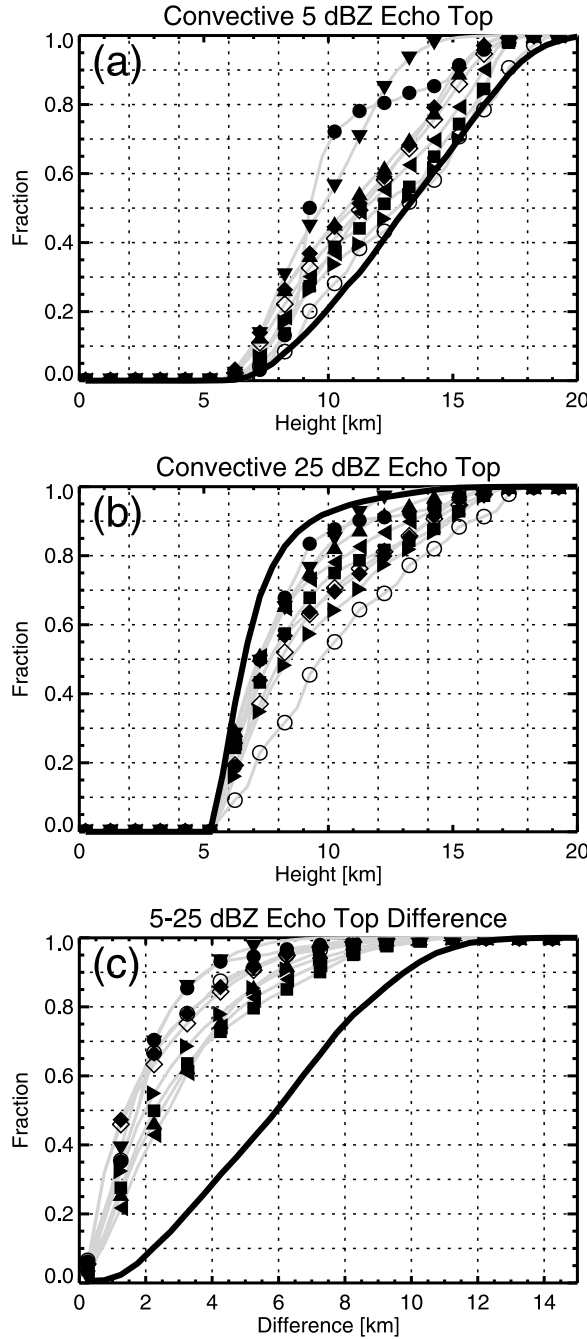


Figure 10. Observed and simulated convective radar reflectivity echo top normalized cumulative distributions for (a) 5 dBZ and (b) 25 dBZ. (c) The cumulative distributions of the difference between 5 dBZ and 25 dBZ echo tops. With the focus on deeper convective regions, samples are limited to columns that have at least a 25 dBZ echo at 5.5 km or higher. Models are represented by symbols (see Table 1), and the thick black lines represent observations from the CPOL radar.

each other and observations is approximately the same no matter whether the 6 day period is split into individual precipitation events (not shown) or relatively quiet periods with very little precipitation. The MESONH-2 simulation has almost continuous very cold brightness temperatures,

which differs from other model simulations. The MESONH-1, UKMO-2M, and SAM-B simulations also produce excessively cold brightness temperatures. Observations show that approximately half of brightness temperatures are colder than 235 K. For the MESONH-2 simulation, the median T_b is about 205 K, and for the MESONH-1, UKMO-2M, and SAM-B simulations, 225 K. The difference between MTSAT and these four simulations increases at warmer brightness temperatures, consistent with the simulations being too uniform. These results would not have been guessed from the MESONH radar reflectivity results given that those simulations have some of the weakest radar reflectivity echoes aloft of all of the simulations. These results are, however, consistent with the uniformity of radar reflectivity echo tops in SAM-B. Despite the overabundance of cold brightness temperatures in these four simulations, all model simulations except for the MESONH-2 simulation have fewer samples than observed at brightness temperatures less than 210 K. On the other end of the spectrum, the UKMO-2 and DHARMA-S simulations are offset to warmer than observed brightness temperatures throughout the distribution. The DHARMA-B simulation is offset from observations at cold brightness temperatures but approximately the same as observed at temperatures warmer than 250 K. The median T_b for the DHARMA-B simulation and UKMO-2 simulation is about 245 K and for the DHARMA-S simulation, 250 K. The SAM-S simulation is fairly close to observations with a slightly larger offset at very cold brightness temperatures. The simulation closest to observations is UKMO-1 despite having the coarsest vertical resolution and one-moment microphysics.

5. Discussion

[38] There are substantial differences between most observed and simulated precipitation and cloud structure properties examined. Radar reflectivity differences can result from a

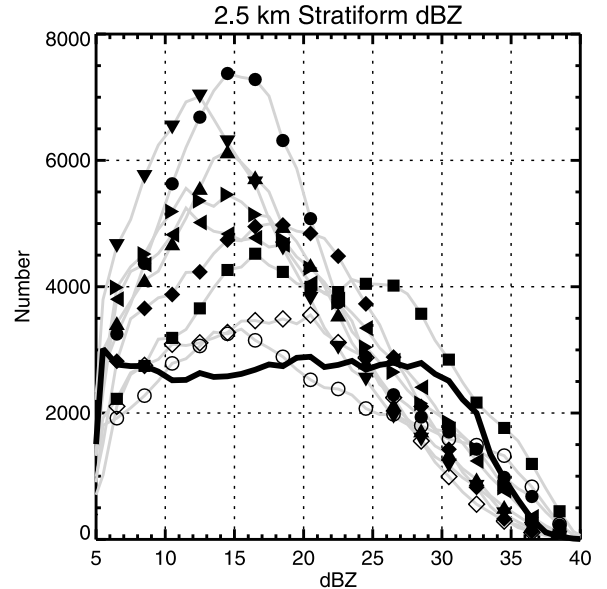


Figure 11. Histogram of observed and simulated stratiform radar reflectivity at 2.5 km. Models are represented by symbols (see Table 1), and the thick black line represents observations from the CPOL radar.

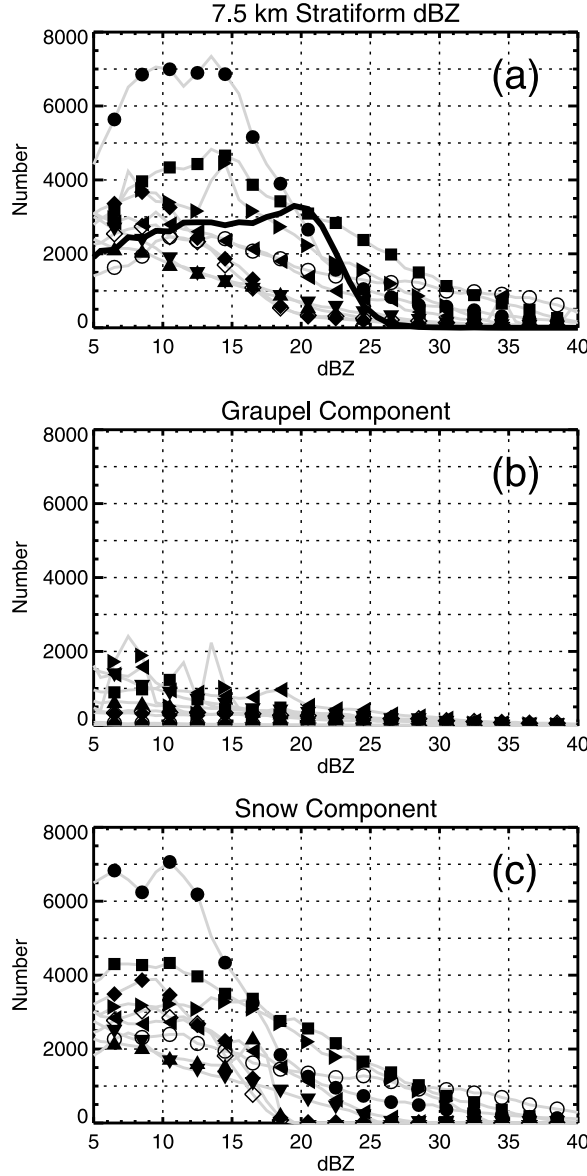


Figure 12. Histograms of (a) 7.5 km observed and simulated stratiform radar reflectivity, (b) 7.5 km simulated graupel radar reflectivity, and (c) 7.5 km simulated snow radar reflectivity. Models are represented by symbols (see Table 1), and the thick black lines represent observations from the CPOL radar.

number of factors including hydrometeor water content and the assumed density and size distribution of each hydrometeor species. Detailed analysis of interactive dynamical and microphysical processes leading to such differences will be the focus of part 2, but a comparison of several model microphysical properties is provided here to explain several of the radar reflectivity differences between models and guide the more detailed analyses to come.

[39] Figure 16 shows normalized cumulative distributions of simulated convective graupel radar reflectivity, ice water content, number concentration, and mass mean melted diameter for all grid points at which the graupel radar reflectivity is at least 5 dBZ and the temperature is less than 0°C. The DHARMA simulations produce the highest graupel radar

reflectivity at all percentiles, whereas the simulations employing two-moment schemes and the MESONH simulations group together at lower reflectivity values. These distributions are clearly not highly correlated with the graupel ice

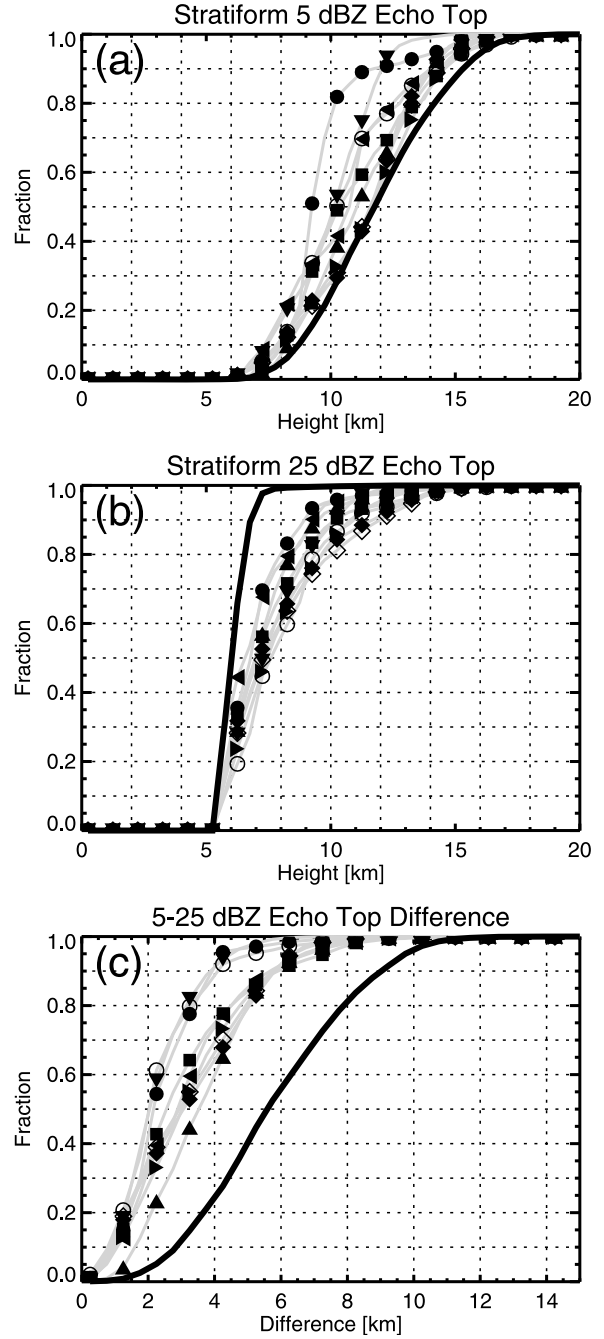


Figure 13. Observed and simulated stratiform radar reflectivity echo top normalized cumulative distributions for (a) 5 dBZ and (b) 20 dBZ. (c) The cumulative distributions of the difference between 5 dBZ and 20 dBZ echo tops. With the focus on well-developed stratiform regions, samples are limited to columns that have at least a 20 dBZ echo at 5.5 km or higher. This also acts to eliminate possible bright band effects in observations. Models are represented by symbols (see Table 1), and the thick black lines represent observations from the CPOL radar.

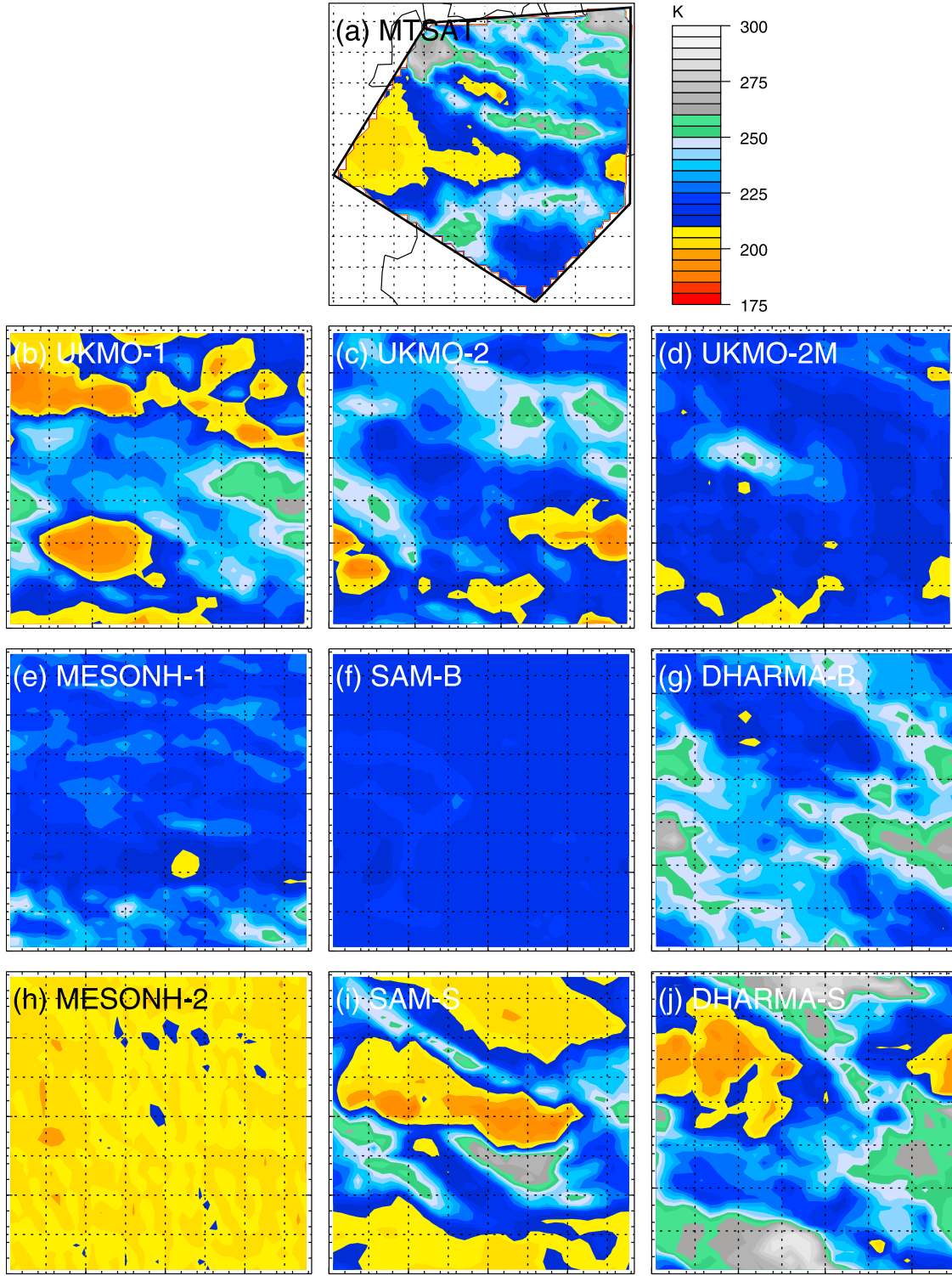


Figure 14. Representative plots of observed and simulated $10.8\text{ }\mu\text{m}$ IR brightness temperatures from the MTSAT satellite at 0300 UTC 20 January 2006: (a) MTSAT, (b) UKMO-1, (c) UKMO-2, (d) UKMO-2M, (e) MESONH-1, (f) SAM-B, (g) DHARMA-B, (h) MESONH-2, (i) SAM-S, and (j) DHARMA-S.

water content distributions shown in Figure 16b because of very different assumptions in size distributions characteristics between different microphysics schemes. The MESONH simulations have the highest graupel ice water contents for grid points with graupel radar reflectivity greater than 5 dBZ

despite having the lowest reflectivities of the one-moment schemes because MESONH has the highest number concentrations of any scheme in Figure 16c. Therefore, Figure 16d shows that the mass mean melted diameters for MESONH graupel are smallest. The other one-moment schemes have

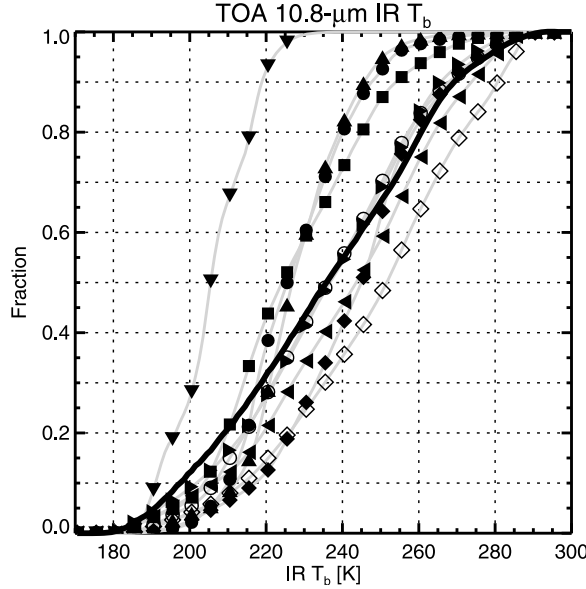


Figure 15. Observed and simulated MTSAT 10.8 μm top-of-atmosphere IR brightness temperature normalized cumulative distributions. Models are represented by symbols (see Table 1), and the thick black line represents observations from MTSAT.

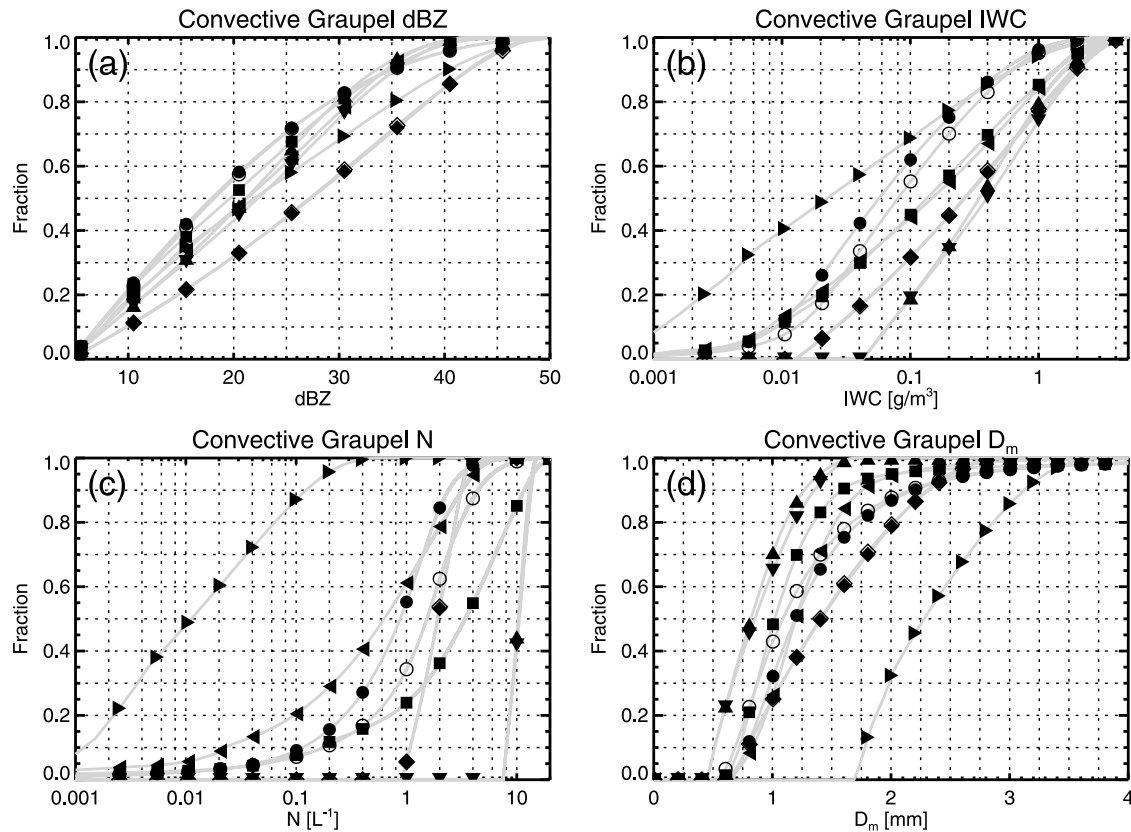


Figure 16. Normalized cumulative distributions of simulated convective graupel (a) radar reflectivity, (b) ice water content, (c) number concentration, and (d) mass mean diameter. Results are filtered to only include grid points at which the graupel radar reflectivity is at least 5 dBZ and the temperature is less than 0°C. Symbols are defined in Table 1.

larger mass mean melted diameters consistent with lower number concentrations rather than higher ice water contents. Recall that MESONH does not grossly overestimate convective radar reflectivity aloft like other one-moment simulations.

[40] All simulations assume a generalized gamma distribution for graupel with the following form:

$$N(D) = N_0 D^\mu e^{-\lambda D},$$

where N_0 is the intercept parameter, μ is the shape parameter, and λ is the slope parameter. Table 6 shows the graupel size distribution parameters for each simulation. N_0 is constant for the *Grabowski* [1999] scheme used in DHARMA and diagnostically determined as a function of λ for all of the one-moment schemes. For two-moment schemes,

$$N_0 = \frac{N \lambda^{\mu+1}}{\Gamma(\mu+1)},$$

where N is the prognostic number concentration. In all schemes, λ is dependent on the prognostic mass mixing ratio. UKMO-1 is an outlier in both mass mean melted diameter and number concentration because it uses a shape factor (μ) of 2.5. The only other simulation with a nonzero shape factor is UKMO-2, but number concentration is predicted in that simulation. The shape parameter is a measure of the dispersion of the size distribution. Simply put,

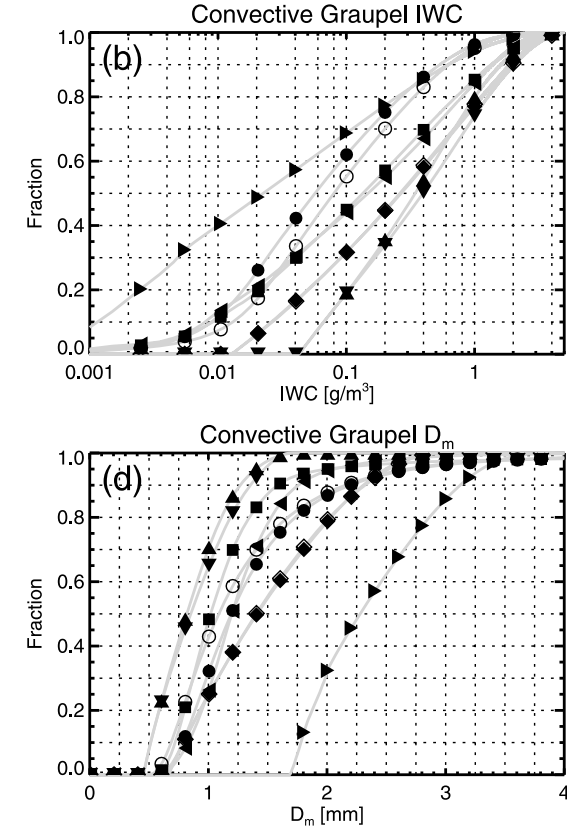


Table 6. The Parameters Necessary for the Gamma Distribution Used for Graupel by All Simulations^a

Model	Graupel Size Distribution Parameters				
	Density	m-D	N ₀	μ	λ
DHARMA	400 kg/m ³	$m = \frac{\pi}{6} \rho_g D^3$	4e6	0	$\left[\frac{\pi \rho_g N_0 \Gamma(4)}{6 \rho_0 q_g} \right]^{\frac{1}{4}}$
MESONH	Variable	$m = 19.6 D_{\max}^{2.8}$	5e5 λ ^{0.5}	0	$\left[\frac{(19.6)(5e5) \Gamma(3.8)}{\rho_0 q_g} \right]^{\frac{1}{3.3}}$
UKMO-1	500 kg/m ³	$m = \frac{\pi}{6} \rho_g D^3$	5e25 λ ⁻⁴	2.5	$\left[\frac{\pi \rho_g (5e25) \Gamma(6.5)}{6 \rho_0 q_g} \right]^{\frac{1}{10.5}}$
UKMO-2	500 kg/m ³	$m = \frac{\pi}{6} \rho_g D^3$	$\frac{\rho_0 N \lambda^{3.5}}{\Gamma(3.5)}$	2.5	$\left[\frac{\pi \rho_g N \Gamma(6.5)}{6 \rho_0 \Gamma(3.5)} \right]^{\frac{1}{3}}$
SAM/UKMO-2M	400 kg/m ³	$m = \frac{\pi}{6} \rho_g D^3$	$\rho_0 N \lambda$	0	$\left[\frac{\pi \rho_g N \Gamma(4)}{6 q_g} \right]^{\frac{1}{3}}$

^aMass-diameter (m-D) relations are shown with the intercept parameter (N_0), the shape parameter (μ), and the slope parameter (λ). For MESONH, particles are nonspherical and thus the m-D relation is in terms of maximum dimension. Notation: ρ_g , graupel density; ρ_0 , air density; and q_g , graupel mass mixing ratio.

increasing shape parameter results in lower number concentrations of smaller particles and increased number concentrations of larger particles. This nonzero shape factor has implications for snow as well. Table 7 shows snow size distribution parameters for each simulation. The Grabowski [1999] microphysics scheme used in the DHARMA simulations is unique in that it has a lognormal distribution for snow based on tropical cirrus observations of McFarquhar and Heymsfield [1997], whereas all other schemes have gamma distributions. MESONH is the only model that uses variable density because of its assumption of nonspherical particles.

[41] The simulations that use Morrison two-moment microphysics and the UKMO-1 simulation have large peaks in excessively high convective snow radar reflectivity, and this shows in that those simulations have far more occurrences of high snow reflectivity in Figure 17a. Figures 17b, 17c, and 17d show normalized cumulative distributions of convective snow ice water content, number concentration, and mass mean melted diameter. As with graupel, the simulations with high radar reflectivity also have the largest mass mean melted diameters. The mass mean melted diameter distributions for two-moment schemes cover a larger range of diameters due to the ability to predict number concentration. This ability also allows a broader range of ice water contents and number concentrations than the one-moment schemes used in MESONH and DHARMA. UKMO-1 is the only one-moment simulation that covers a large range of ice water contents and number concentrations due to a nonzero shape parameter. This suggests that a diagnostically varying shape parameter may be required to properly simulate the range of ice water contents and number concentrations associated with precipitation-sized ice.

[42] In Figure 18, normalized cumulative distributions for snow are again shown but for stratiform regions. The order of distributions is very close to those for convective snow. Relative to convective snow ice water content, the stratiform snow ice water content for all two-moment schemes and UKMO-1 significantly drops, whereas it only slightly drops for MESONH and DHARMA. In fact, DHARMA has the highest stratiform snow ice water contents but the lowest stratiform snow radar reflectivity because of extremely high number concentrations that limit the size of snow. UKMO-1

again has the lowest number concentrations due to the high shape parameter allowing for higher reflectivities closer to observations. Whereas the nonspherical mass-dimension relationships used in MESONH aided those simulations with respect to graupel radar reflectivity, they produce snow reflectivities that are too low. This is clearly shown in Figure 19, which shows radar reflectivity as a function of ice water content for graupel and snow.

[43] One-moment microphysics schemes produce single lines in Figure 19 because each water content has but one size distribution and hence one radar reflectivity in these treatments (unlike more complex one-moment schemes, with diagnostic intercepts, such as Thompson *et al.*'s [2004]). Two-moment schemes, however, allow for different size distributions for a given ice water content and hence, such schemes are depicted by frequency distributions in which the shading contours are logarithmically spaced. Figure 19 reaffirms the differences in size distribution assumptions. For graupel in Figures 19a, 19b, and 19c, MESONH has the lowest radar reflectivity for any given ice water content, but the MESONH convective radar reflectivity agrees much better with observations than the other simulations. For both graupel and snow, the range of reflectivity possibilities for a given ice water content is very large as shown in the shadings. The slope and values of the relation for UKMO-1 snow is closest to the two-moment schemes, but clearly aggregation leads to a spread to higher reflectivities in the two-moment schemes that the one-moment schemes cannot produce with fixed shape parameters in the size distribution. In reality, snow aggregates as it approaches the melting level [Houze and Churchill, 1987; Heymsfield *et al.*, 2002; Stith *et al.*, 2002] leading to small concentrations of large snow particles. Microphysics schemes, such as two-moment schemes, that have the ability to predict a large spread of reflectivity values for a given ice water content have the ability to better predict the observed radar reflectivity distribution. However, simulations with the two-moment Morrison scheme generally produce snow particles that are too large. This is not to say that all two-moment schemes have this problem as very large snow particles are not nearly as common in the UKMO two-moment scheme (shaded in Figures 15c and 15f), which has far fewer samples of high radar reflectivity at very low ice water contents for both graupel and snow.

Table 7. The Parameters Necessary for the Gamma Distribution Used for Snow by MESONH, UKMO, and SAM^a

Model	Snow Size Distribution Parameters				
	Density	m-D	N ₀	μ	λ
DHARMA	100 kg/m ³	$m = \frac{\pi}{6} \rho_s D^3$	—	—	$\left[\frac{(0.02)(5) \Gamma(2.9)}{\rho_0 q_s} \right]^{\frac{1}{3}}$
MESONH	Variable	$m = 0.02 D_{\max}^{1.9}$	5λ ²	0	$\left[\frac{\rho_0}{\rho_0 q_s} \right]^{\frac{1}{0.9}}$
UKMO-1	100 kg/m ³	$m = \frac{\pi}{6} \rho_s D^3$	2e27 λ ^{-3.5}	2.5	$\left[\frac{\pi \rho_s (2e27) \Gamma(6.5)}{6 \rho_0 q_s} \right]^{\frac{1}{10}}$
UKMO-2	100 kg/m ³	$m = \frac{\pi}{6} \rho_s D^3$	$\frac{\rho_0 N \lambda^{3.5}}{\Gamma(3.5)}$	2.5	$\left[\frac{\pi \rho_s N \Gamma(6.5)}{6 q_s \Gamma(3.5)} \right]^{\frac{1}{3}}$
SAM/UKMO-2M	100 kg/m ³	$m = \frac{\pi}{6} \rho_s D^3$	$\rho_0 N \lambda$	0	$\left[\frac{\pi \rho_s N \Gamma(4)}{6 q_s} \right]^{\frac{1}{3}}$

^aMass-diameter (m-D) relations are shown with the intercept parameter (N_0), the shape parameter (μ), and the slope parameter (λ). For MESONH, particles are nonspherical and thus the m-D relation is in terms of maximum dimension. For DHARMA, the distribution is lognormal and shown by McFarquhar and Heymsfield [1997]. Notation: ρ_s , snow density; ρ_0 , air density; q_s , graupel mass mixing ratio.

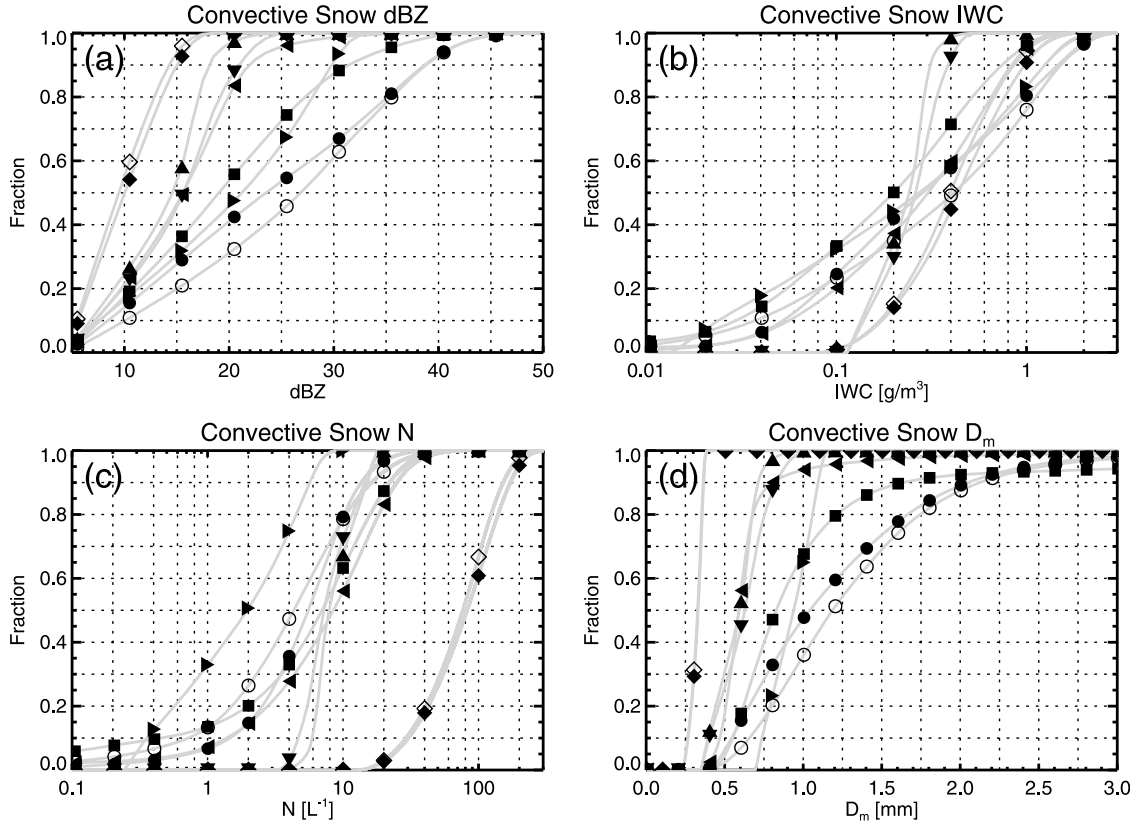


Figure 17. Normalized cumulative distributions of simulated convective snow (a) radar reflectivity, (b) ice water content, (c) number concentration, and (d) mass mean diameter. Results are filtered to only include grid points at which the snow radar reflectivity is at least 5 dBZ and the temperature is less than 0°C. Symbols are defined in Table 1.

[44] The same microphysics scheme can produce very different hydrometeor water contents and size distributions with different dynamics treatments as shown by the difference between SAM-B and UKMO-2M. UKMO-2M produces far more graupel and less snow than SAM-B. That said, different microphysics schemes with the same dynamics treatment can lead to very different water contents and size distributions as seen in the UKMO-1 and UKMO-2 results. UKMO-2 produces far more graupel than UKMO-1 and yet, UKMO-1 tends to have higher reflectivities aloft in both convective and stratiform regions. This is but one example that shows that although it is obvious that radar reflectivity aloft depends on ice water content for any one simulation, Figures 16–19 collectively show that differences in radar reflectivity across nine simulations are more dependent on differences in assumed size distribution properties, such as intercept, shape, and slope parameter.

6. Conclusions

[45] An essential component to properly evaluating and improving cloud-resolving model simulations of tropical convective precipitation systems is comparing precipitation and cloud structure with observations at convective scales. Whereas previous literature has strictly focused on convective and stratiform structures in individual models or larger-scale properties in several models, this study uniquely combines these two approaches. This first part of a two part

study focuses on establishing radar reflectivity and IR Tb differences between models and observations while relating these differences to hydrometeor properties and assumptions.

[46] Our study partially agrees with previous studies [e.g., Blossey *et al.*, 2007; Lang *et al.*, 2007; Li *et al.*, 2008; Matsui *et al.*, 2009] that conclude that one-moment microphysics schemes produce excessive amounts of large graupel. This is certainly true of the DHARMA and UKMO-1 simulations, but the MESONH simulations show that assuming nonspherical particles with varying density and altering the mass-dimension relationship for graupel particles can lead to convective radar reflectivities aloft that are much closer to those observed. Simulations using the Morrison two-moment microphysics scheme show that snow rather than graupel can also lead to excessively high radar reflectivity. These excessively large snow particles exist in both convective and stratiform regions, although this is not a symptom of all two-moment schemes, as the UKMO-2 produces much lower reflectivity values for snow. All baseline simulations produce expansive stratiform regions larger than those in observations but such areal expanse cannot make up for a preponderance of unrealistically low rain rates in all simulations. Some studies [e.g., Morrison *et al.*, 2009] have shown that when two moments of the rain size distribution are predicted, higher stratiform rain rates are produced, but that was not the case in this study. Simulated convective rainfall makes up for the shortfall in stratiform rainfall through larger than observed convective area.

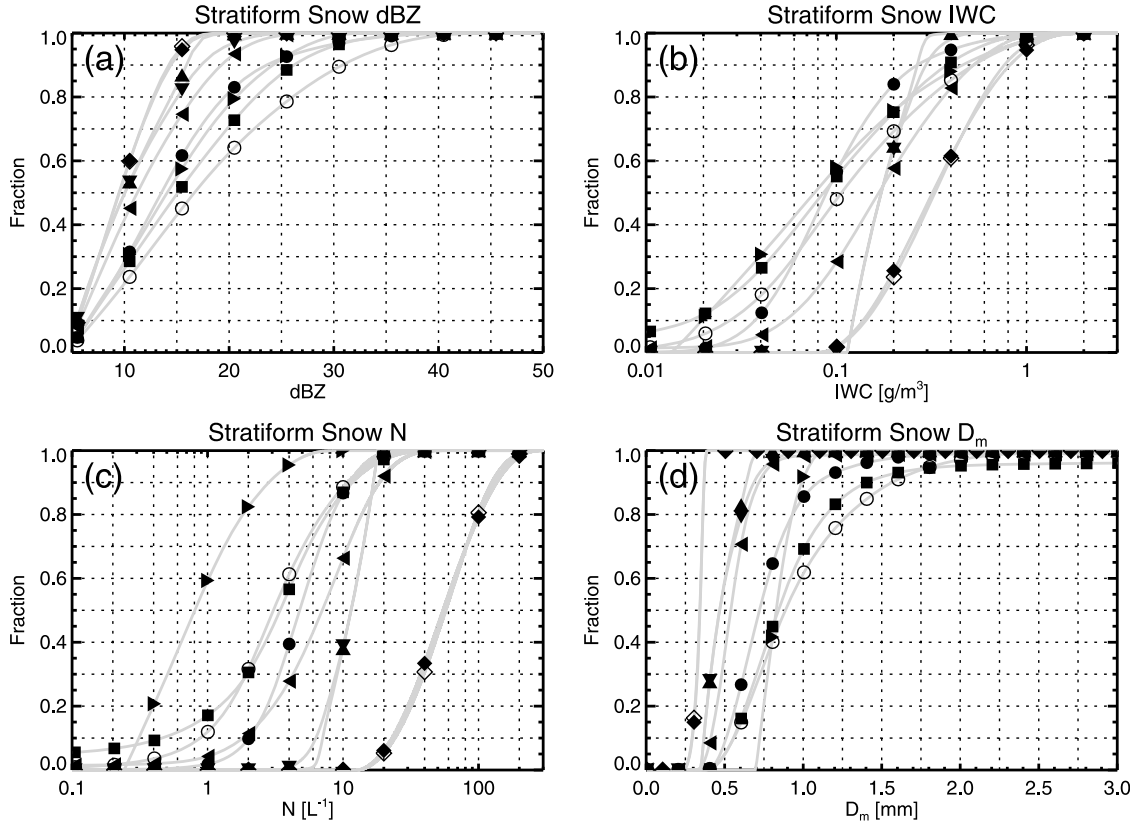


Figure 18. Normalized cumulative distributions of simulated stratiform snow (a) radar reflectivity, (b) ice water content, (c) number concentration, and (d) mass mean diameter. Results are filtered to only include grid points at which the snow radar reflectivity is at least 5 dBZ and the temperature is less than 0°C. Symbols are defined in Table 1.

[47] Distributions of ice water content, number concentration, and mass mean melted diameter for both graupel and snow show that varying the intercept and shape parameters of a gamma distribution has much larger effects on radar reflectivity than varying the ice water content. There is evidence that a shape parameter greater than 0 can reduce the biases present in both one-moment and two-moment schemes. This agrees with previous literature [Milbrandt and Yau, 2005] that shows that a diagnostically varying shape parameter (μ) yields much better results because μ has a significant effect on sedimentation and instantaneous growth rates of hydrometeors. Variable density and diagnostic relations between N_0 and λ also lead to very different size distributions and radar reflectivity for given ice water contents. Unfortunately, no combination of these variables in this intercomparison leads to the observed decrease in radar reflectivity with height aloft in convective and stratiform regions.

[48] In addition to radar reflectivity structure, a comparison of simulated infrared brightness temperatures showed that some simulations produced overly abundant cold temperatures whereas others produced warmer than observed temperatures. These results were not highly correlated with the radar reflectivity echo top distributions as the $10.7\ \mu\text{m}$ brightness temperature is very sensitive to small ice particles, of which some simulations had expansive regions and others did not. The degree to which the abundant cold brightness temperatures are due to model forcing or due to

dynamical-microphysical processes will be investigated in part II. UKMO-1 performs the best of all simulations by almost exactly replicating the normalized cumulative distribution of IR T_b . In fact, in rain rate statistics, radar reflectivity statistics, and IR T_b statistics, there is not a clear superiority of two-moment schemes over one-moment schemes in reproducing observations. Two-moment schemes tend to have an entirely different set of problems, although their potential ability to be superior is evident as shown in the large ranges of ice water content, number concentration, and mass mean melted diameter possible for precipitation sized ice.

[49] Nudged sensitivity simulations were performed to investigate accumulation of error resulting from long-term application of forcing or possible inaccuracies associated with applying forcing uniformly over a large area. The two sensitivity simulations produce far less stratiform area than all baseline simulations bringing them much closer to observations. This improvement also shows in higher frequency of warm brightness temperatures compared to corresponding baseline simulations. Differences are not limited to stratiform regions as the sensitivity simulations have higher convective radar reflectivity aloft with deeper convective and stratiform regions compared to their baselines. These results suggest that error due to the idealized forcing in the baseline simulations may lead to excessive cloudiness, excessive stratiform area, and potentially weaker convective updrafts.

[50] Convective and stratiform radar reflectivity characteristics and IR T_b characteristics are often very similar for

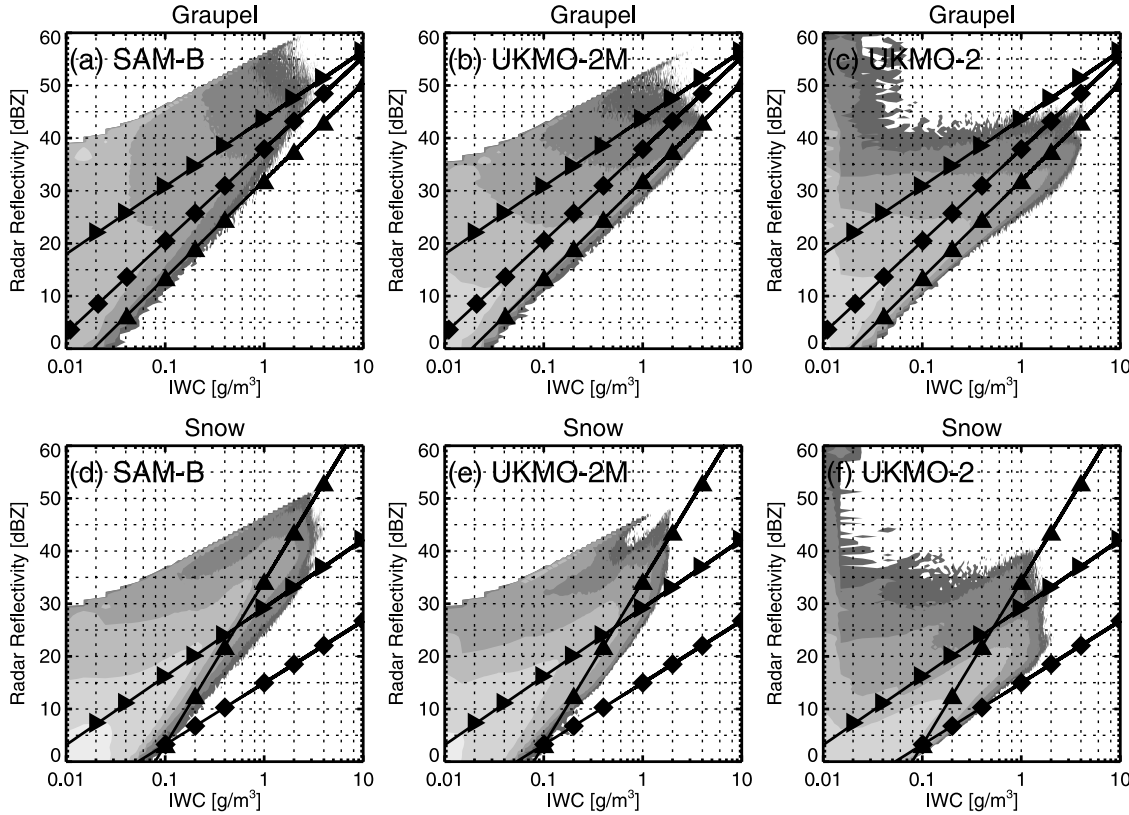


Figure 19. Simulated radar reflectivity as a function of water content for (a, b, and c) graupel and (d, e, and f) snow. Symbols are defined in Table 1. The shading in Figures 19a and 19d is from SAM-B results, with each shading increasing by an order of magnitude starting with 1 to 10 samples per bin for the darkest shading increasing to 100,000 or more samples per bin for the brightest shading in Figures 19d and 19e; shading in Figures 19b and 19e is from UKMO-2M results; and shading in Figures 19c and 19f is from UKMO-2.

a given model (e.g., UKMO-1 and UKMO-2) or given microphysics scheme (e.g., SAM-B and UKMO-2M), which implicates the importance of both dynamics and microphysics in the cloud and precipitation structural differences found. To study these interactions, the evolution of convective systems that develop stratiform regions will be examined through higher temporal resolution simulations in part 2. It should be kept in mind throughout, however, that assumptions inherent to the model forcing and boundary conditions also lead to systematic errors. This is currently being investigated through detailed comparisons of these CRM results with results obtained in the TWP-ICE limited area model (LAM) intercomparison study, which employs open boundary conditions and nested domains.

[51] **Acknowledgments.** This research was supported by the Department of Energy's Atmospheric Research Program, award DEFG0208ER64557, program manager Kiran Alapaty. Special thanks are given to Peter May at the Centre for Australian Weather and Climate Research and the Australian Bureau of Meteorology for providing the CPOL radar data, Pat Minnis and his group at NASA Langley Research Center for archiving the MTSAT data, and the JCSDA and model developers for providing the CRTM. DHARMA simulations were supported by DOE Office of Science, Office of Biological and Environmental Research, through interagency agreement DE-AI02-06ER64173 and contract DE-FG03-02ER63337, the NASA Radiation Sciences Program, the DOE National Energy Research Scientific Computing Center, and the NASA Advanced Supercomputing Division.

References

- Ackerman, A., O. Toon, D. Stevens, A. Heymsfield, V. Ramanathan, and E. Welton (2000), Reduction of tropical cloudiness by soot, *Science*, 288(5468), 1042–1047, doi:10.1126/science.288.5468.1042.
- Bechtold, P., et al. (2000), A GCSS model intercomparison for a tropical squall line observed during TOGA-COARE. II: Intercomparison of single-column models and a cloud-resolving model, *Q. J. R. Meteorol. Soc.*, 126(564), 865–888.
- Belamari, S. (2005), Report on uncertainty estimates of an optimal bulk formulation for surface turbulent fluxes, report, Mar. Environ. and Security for the Eur. Area Integrated Proj., Plouzané, France.
- Biggerstaff, M. I., and R. A. Houze Jr. (1991), Kinematic and precipitation structure of the 10–11 June 1985 squall line, *Mon. Weather Rev.*, 119(12), 3034–3065, doi:10.1175/1520-0493(1991)119<3034:KAPSOT>2.0.CO;2.
- Blossay, P. N., C. S. Bretherton, J. Cetrone, and M. Kharoutdinov (2007), Cloud-resolving model simulations of KWAJEX: Model sensitivities and comparisons with satellite radar observations, *J. Atmos. Sci.*, 64(5), 1488–1508, doi:10.1175/JAS3982.1.
- Chen, Y., F. Weng, Y. Han, and Q. Liu (2008), Validation of the Community Radiative Transfer Model by using CloudSat data, *J. Geophys. Res.*, 113, D00A03, doi:10.1029/2007JD009561.
- Colella, P., and P. Woodward (1984), The piecewise parabolic method (PPM) for gas-dynamical simulations, *J. Comput. Phys.*, 54(1), 174–201, doi:10.1016/0021-9991(84)90143-8.
- Collins, W. D., J. Wang, J. T. Kiehl, G. J. Zhang, D. I. Cooper, and W. E. Eichinger (1997), Comparison of tropical ocean–atmosphere fluxes with the NCAR Community Climate Model CCM3, *J. Clim.*, 10(12), 3047–3058, doi:10.1175/1520-0442(1997)010<3047:COTAOF>2.0.CO;2.
- Cuxart, J., P. Bougeault, and J.-L. Redelsperger (2000), A turbulence scheme allowing for mesoscale and large-eddy simulations, *Q. J. R. Meteorol. Soc.*, 126(562), 1–30, doi:10.1002/qj.49712656202.

- Deardorff, J. W. (1970), A numerical study of three-dimensional turbulent channel flow at large Reynolds number, *J. Fluid Mech.*, **41**, 453–480, doi:10.1017/S0022112070000691.
- Del Genio, A. D., and W. Kovari (2002), Climatic properties of tropical precipitating convection under varying environmental conditions, *J. Clim.*, **15**(18), 2597–2615, doi:10.1175/1520-0442(2002)015<2597:CPOTPC>2.0.CO;2.
- Del Genio, A. D., and J. Wu (2010), The role of entrainment in the diurnal cycle of continental convection, *J. Clim.*, **23**(10), 2722–2738, doi:10.1175/2009JCLI3340.1.
- Edwards, J. M., and A. Slingo (1996), Studies with a flexible new radiation code. I: Choosing a configuration for a large-scale model, *Q. J. R. Meteorol. Soc.*, **122**(531), 689–719, doi:10.1002/qj.49712253107.
- Fridlind, A., A. Ackerman, J. Petch, P. Field, A. Hill, G. McFarquhar, S. Xie, and M. Zhang (2010), ARM/GCSS/SPARC TWP-ICE CRM Intercomparison Study, *NASA Tech. Memo.*, TM-2010-215858.
- Ghan, S. J., et al. (2000), A comparison of single column model simulations of summertime midlatitude continental convection, *J. Geophys. Res.*, **105**(D2), 2091–2124, doi:10.1029/1999JD900971.
- Grabowski, W. W. (1999), A parameterization of cloud microphysics for long-term cloud-resolving modeling of tropical convection, *Atmos. Res.*, **52**(1–2), 17–41, doi:10.1016/S0169-8095(99)00029-0.
- Grabowski, W. W., et al. (2006), Daytime convective development over land: A model intercomparison based on LBA observations, *Q. J. R. Meteorol. Soc.*, **132**(615), 317–344, doi:10.1256/qj.04.147.
- Gregory, D., J. J. Morcrette, C. Jakob, A. M. Beljaars, and T. Stockdale (2000), Revision of convection, radiation and cloud schemes in the ECMWF model, *Q. J. R. Meteorol. Soc.*, **126**(566), 1685–1710.
- Han, Y., P. van Delst, Q. Liu, F. Weng, B. Yan, R. Treadon, and J. Derber (2006), Community Radiative Transfer Model (CRTM): Version 1, *Tech. Rep. NESDIS 122*, NOAA, Washington, D. C.
- Heymsfield, A. J., A. Bansemer, P. R. Field, S. L. Durden, J. L. Stith, J. E. Dye, W. Hall, and C. A. Grainger (2002), Observations and parameterizations of particle size distributions in deep tropical cirrus and stratiform precipitating clouds: Results from in situ observations in TRMM field campaigns, *J. Atmos. Sci.*, **59**(24), 3457–3491, doi:10.1175/1520-0469(2002)059<3457:OAPOPS>2.0.CO;2.
- Houghton, H. G. (1968), On precipitation mechanisms and their artificial modification, *J. Appl. Meteorol.*, **7**(5), 851–859, doi:10.1175/1520-0450(1968)007<0851:OPMATA>2.0.CO;2.
- Houze, R. A., Jr. (1982), Cloud clusters and large-scale vertical motions in the tropics, *J. Meteorol. Soc. Jpn.*, **60**(1), 396–410.
- Houze, R. A., Jr. (1989), Observed structure of mesoscale convective systems and implications for large-scale heating, *Q. J. R. Meteorol. Soc.*, **115**(487), 425–461, doi:10.1002/qj.49711548702.
- Houze, R. A., Jr. (1997), Stratiform precipitation in regions of convection: A meteorological paradox?, *Bull. Am. Meteorol. Soc.*, **78**(10), 2179–2196, doi:10.1175/1520-0477(1997)078<2179:SPIROC>2.0.CO;2.
- Houze, R. A., Jr., and D. D. Churchill (1987), Mesoscale organization and cloud microphysics in a Bay of Bengal depression, *J. Atmos. Sci.*, **44**(14), 1845–1868, doi:10.1175/1520-0469(1987)044<1845:MOACMI>2.0.CO;2.
- Huang, H.-L., P. Yang, H. Wei, B. A. Baum, Y. Hu, P. Antonelli, and S. A. Ackerman (2004), Inference of ice cloud properties from high spectral resolution infrared observations, *IEEE Trans. Geosci. Remote Sens.*, **42**(4), 842–853, doi:10.1109/TGRS.2003.822752.
- Jakob, C., and G. Tselioudis (2003), Objective identification of cloud regimes in the Tropical Western Pacific, *Geophys. Res. Lett.*, **30**(21), 2082, doi:10.1029/2003GL018367.
- Johnson, R. H. (1984), Partitioning tropical heat and moisture budgets into cumulus and mesoscale components: Implications for cumulus parameterization, *Mon. Weather Rev.*, **112**(8), 1590–1601, doi:10.1175/1520-0493(1984)112<1590:PTHAM>2.0.CO;2.
- Keenan, T. D., and R. E. Carbone (1992), A preliminary morphology of precipitation systems in tropical northern Australia, *Q. J. R. Meteorol. Soc.*, **118**(504), 283–326, doi:10.1002/qj.49711850406.
- Keenan, T. D., K. Glasson, F. Cummings, T. S. Bird, J. Keeler, and J. Lutz (1998), The BMRC/NCAR C-band polarimetric (C-POL) radar system, *J. Atmos. Oceanic Technol.*, **15**(4), 871–886, doi:10.1175/1520-0426(1998)015<0871:TBNCBP>2.0.CO;2.
- Khairoutdinov, M., and D. Randall (2003), Cloud resolving modeling of the ARM summer 1997 IOP: Model formulation, results, uncertainties, and sensitivities, *J. Atmos. Sci.*, **60**(4), 607–625, doi:10.1175/1520-0469(2003)060<0607:CRMOTA>2.0.CO;2.
- Kiehl, J. T., J. J. Hack, G. B. Bonan, B. A. Boville, D. L. Williamson, and P. J. Rasch (1998), The National Center for Atmospheric Research Community Climate Model: CCM3, *J. Clim.*, **11**(6), 1131–1149, doi:10.1175/1520-0442(1998)011<1131:TNCFAR>2.0.CO;2.
- Lafore, J. P., et al. (1998), The Meso-NH atmospheric simulation system. Part I: Adiabatic formulation and control simulations, *Ann. Geophys.*, **16**, 90–109, doi:10.1007/s00585-997-0090-6.
- Lang, S., W.-K. Tao, J. Simpson, R. Cifelli, S. Rutledge, W. Olson, and J. Halverson (2007), Improving simulations of convective systems from TRMM LBA: Easterly and westerly regimes, *J. Atmos. Sci.*, **64**(4), 1141–1164, doi:10.1175/JAS3879.1.
- Leonard, B. P., M. K. MacVean, and A. P. Lock (1993), Positivity-preserving numerical schemes for multidimensional advection, *NASA Tech. Memo.*, TM-106055.
- Li, Y., E. J. Zipser, S. K. Krueger, and M. A. Zulauf (2008), Cloud-resolving modeling of deep convection during KWAJEX. Part I: Comparison to TRMM satellite and ground-based observations, *Mon. Weather Rev.*, **136**(7), 2699–2712, doi:10.1175/2007MWR2258.1.
- Lilly, D. K. (1967), The representation of small-scale turbulence in numerical simulation experiments, paper presented at IBM Scientific Computing Symposium on Environmental Sciences, IBM Data Process. Div., White Plains, N. Y.
- Liu, Q., and F. Weng (2006), Advanced doubling–adding method for radiative transfer in planetary atmosphere, *J. Atmos. Sci.*, **63**(12), 3459–3465, doi:10.1175/JAS3808.1.
- Matsui, T., X. Zeng, W.-K. Tao, H. Masunaga, W. S. Olson, and S. Lang (2009), Evaluation of long-term cloud-resolving model simulations using satellite radiance observations and multifrequency satellite simulators, *J. Atmos. Oceanic Technol.*, **26**(7), 1261–1274, doi:10.1175/2008JTECHA1168.1.
- May, P. T., J. H. Mather, G. Vaughan, K. N. Bower, C. Jakob, G. M. McFarquhar, and G. G. Mace (2008), The Tropical Warm Pool International Cloud Experiment, *Bull. Am. Meteorol. Soc.*, **89**(5), 629–645, doi:10.1175/BAMS-89-5-629.
- McFarquhar, G. M., and A. J. Heymsfield (1997), Parameterization of tropical cirrus ice crystal size distributions and implications for radiative transfer: Results from CEPEX, *J. Atmos. Sci.*, **54**(17), 2187–2200, doi:10.1175/1520-0469(1997)054<2187:POTCIC>2.0.CO;2.
- Meyers, M. P., P. J. DeMott, and W. R. Cotton (1992), New primary ice nucleation parameterizations in an explicit cloud model, *J. Appl. Meteorol.*, **31**(7), 708–721, doi:10.1175/1520-0450(1992)031<0708:NPINPI>2.0.CO;2.
- Milbrandt, J. A., and M. K. Yau (2005), A multimoment bulk microphysics parameterization. Part I: Analysis of the role of the spectral shape parameter, *J. Atmos. Sci.*, **62**(9), 3051–3064, doi:10.1175/JAS3534.1.
- Mlawer, E. J., S. J. Taubman, P. D. Brown, M. J. Iacono, and S. A. Clough (1997), Radiative transfer for inhomogeneous atmospheres: RRTM, a validated correlated-k model for the longwave, *J. Geophys. Res.*, **102**(D14), 16,663–16,682, doi:10.1029/97JD00237.
- Moncrieff, M. W., S. K. Krueger, D. Gregory, J.-L. Redelsperger, and W.-K. Tao (1997), GEWEX Cloud System Study (GCSS) Working Group 4: Precipitating convective cloud systems, *Bull. Am. Meteorol. Soc.*, **78**(5), 831–845, doi:10.1175/1520-0477(1997)078<0831:GCSSGW>2.0.CO;2.
- Monin, A. S., and A. M. Obukhov (1954), Basic laws of turbulent mixing in the surface layer of the atmosphere, *Tr. Geofiz. Inst. Akad. Nauk SSSR*, **24**(151), 163–187.
- Morrison, H., G. Thompson, and V. Tatarkii (2009), Impact of cloud microphysics on the development of trailing stratiform precipitation in a simulated squall line: Comparison of one- and two-moment schemes, *Mon. Weather Rev.*, **137**(3), 991–1007, doi:10.1175/2008MWR2556.1.
- Neale, R., and J. Slingo (2003), The maritime continent and its role in the global climate: A GCM study, *J. Clim.*, **16**(5), 834–848, doi:10.1175/1520-0442(2003)016<0834:TMCAIR>2.0.CO;2.
- Petch, J. C., and M. E. B. Gray (2001), Sensitivity studies using a cloud-resolving model simulation of the tropical west Pacific, *Q. J. R. Meteorol. Soc.*, **127**(577), 2287–2306, doi:10.1002/qj.49712757705.
- Petch, J. C., M. Willett, R. Y. Wong, and S. J. Woolnough (2007), Modelling suppressed and active convection: Comparing a numerical weather prediction, cloud-resolving and single-column model, *Q. J. R. Meteorol. Soc.*, **133**(626), 1087–1100, doi:10.1002/qj.109.
- Piacsek, S. A., and G. P. Williams (1970), Conservation properties of convection difference schemes, *J. Comput. Phys.*, **6**(3), 392–405, doi:10.1016/0021-9910(70)90038-0.
- Pinty, J.-P. (2002), A quasi 2-moment microphysical scheme for mixed-phase clouds at mesoscale with sensitivity to aerosols (CCN and IN), paper presented at 11th Conference on Cloud Physics, Am. Meteorol. Soc., Ogden, Utah.
- Pinty, J.-P., and P. Jabouille (1998), A mixed-phase cloud parameterization for use in a mesoscale non-hydrostatic model: Simulations of a squall line and of orographic precipitation, paper presented at Conference on Cloud Physics, Am. Meteorol. Soc., Everett, Wash.
- Randall, D. A., et al. (2003), Confronting models with data: The GEWEX Cloud Systems Study, *Bull. Am. Meteorol. Soc.*, **84**(4), 455–469, doi:10.1175/BAMS-84-4-455.

- Randall, D. A., et al. (2007), Climate models and their evaluation, in *Climate Change 2007: The Physical Science Basis, Contribution of Working Group I to the Fourth Assessment Report of the Intergovernmental Panel on Climate Change*, edited by S. Solomon et al., pp. 589–662, Cambridge Univ. Press, Cambridge, U.K.
- Redelsperger, J.-L., et al. (2000), A GCSS model intercomparison for a tropical squall line observed during TOGA-COARE. Part I: CRM results, *Q. J. R. Meteorol. Soc.*, 126(564), 823–863.
- Rutledge, S. A., and R. A. Houze Jr. (1987), A diagnostic modeling study of the trailing stratiform region of a midlatitude squall line, *J. Atmos. Sci.*, 44(18), 2640–2656, doi:10.1175/1520-0469(1987)044<2640:ADMSOT>2.0.CO;2.
- Shutts, G. J., and M. E. B. Gray (1994), A numerical modeling study of the geostrophic adjustment process following deep convection, *Q. J. R. Meteorol. Soc.*, 120(519), 1145–1178, doi:10.1002/qj.49712051903.
- Smith, P. L. (1984), Equivalent radar reflectivity factors for snow and ice particles, *J. Clim. Appl. Meteorol.*, 23(8), 1258–1260, doi:10.1175/1520-0450(1984)023<1258:ERRFFS>2.0.CO;2.
- Smolarkiewicz, P. K., and W. W. Grabowski (1990), The multidimensional positive definite advection transport algorithm: Nonoscillatory option, *J. Comput. Phys.*, 86(2), 355–375, doi:10.1016/0021-9991(90)90105-A.
- Smull, B. F., and R. A. Houze Jr. (1985), A midlatitude squall line with a trailing region of stratiform rain: Radar and satellite observations, *Mon. Weather Rev.*, 113(1), 117–133, doi:10.1175/1520-0493(1985)113<0117:AMSLWA>2.0.CO;2.
- Steiner, M., R. Houze, and S. E. Yuter (1995), Climatological characterization of three-dimensional storm structure from operational radar and rain gauge data, *J. Appl. Meteorol.*, 34(9), 1978–2007, doi:10.1175/1520-0450(1995)034<1978:CCOTDS>2.0.CO;2.
- Stephens, G. L. (2005), Cloud feedbacks in the climate system: A critical review, *J. Clim.*, 18(2), 237–273, doi:10.1175/JCLI-3243.1.
- Stevens, D. E., and C. S. Bretherton (1996), A forward-in-time advection scheme and adaptive multilevel flow solver for nearly incompressible atmospheric flow, *J. Comput. Phys.*, 129(2), 284–295, doi:10.1006/jcph.1996.0250.
- Stevens, D. E., A. S. Ackerman, and C. S. Bretherton (2002), Effects of domain size and numerical resolution on the simulation of shallow cumulus convection, *J. Atmos. Sci.*, 59(23), 3285–3301, doi:10.1175/1520-0469(2002)059<3285:EODSAN>2.0.CO;2.
- Stith, J. L., J. E. Dye, A. Bansemer, A. J. Heymsfield, C. A. Grainger, W. A. Petersen, and R. Cifelli (2002), Microphysical observations of tropical clouds, *J. Appl. Meteorol.*, 41(2), 97–117, doi:10.1175/1520-0450(2002)041<0097:MOOTC>2.0.CO;2.
- Thompson, G., R. M. Rasmussen, and K. Manning (2004), Explicit forecasts of winter precipitation using an improved bulk microphysics scheme. Part I: Description and sensitivity analysis, *Mon. Weather Rev.*, 132(2), 519–542, doi:10.1175/1520-0493(2004)132<0519:EFOWPU>2.0.CO;2.
- Toon, O. B., C. P. McKay, T. P. Ackerman, and K. Santhanam (1989), Rapid calculation of radiative heating rates and photodissociation rates in inhomogeneous multiple scattering atmospheres, *J. Geophys. Res.*, 94(D13), 16,287–16,301, doi:10.1029/JD094iD13p16287.
- Wang, W., and X. Liu (2009), Evaluating deep updraft formulation in NCAR CAM3 with high-resolution WRF simulations during ARM TWP-ICE, *Geophys. Res. Lett.*, 36, L04701, doi:10.1029/2008GL036692.
- Wang, Y., C. Long, L. Leung, J. Dudhia, S. McFarlane, J. Mather, S. Ghan, and X. Liu (2009), Evaluating regional cloud-permitting simulations of the WRF model for the Tropical Warm Pool International Cloud Experiment (TWP-ICE), Darwin, 2006, *J. Geophys. Res.*, 114, D21203, doi:10.1029/2009JD012729.
- Wapler, K., T. Lane, P. May, C. Jakob, M. Manton, and S. Siems (2010), Cloud-system-resolving model simulations of tropical cloud systems observed during the Tropical Warm Pool-International Cloud Experiment, *Mon. Weather Rev.*, 138(1), 55–73, doi:10.1175/2009MWR2993.1.
- Weill, A., et al. (2003), Toward better determination of turbulent air-sea fluxes from several experiments, *J. Clim.*, 16(4), 600–618, doi:10.1175/1520-0442(2003)016<0600:TABDOT>2.0.CO;2.
- Weng, F., Y. Han, P. van Delst, Q. Liu, and B. Yan (2005), JCSDA Community radiative transfer model (CRTM), paper presented at 14th International ATOVS Study Conference, Int. TOVS Working Group, Beijing, China.
- Willett, M. R., P. Bechtold, D. L. Williamson, J. C. Petch, S. F. Milton, and S. J. Woolnough (2008), Modelling suppressed and active convection: Comparisons between three global atmospheric models, *Q. J. R. Meteorol. Soc.*, 134(636), 1881–1896, doi:10.1002/qj.317.
- Wu, J., A. Del Genio, M. Yao, and A. Wolf (2009), WRF and GISS SCM simulations of convective updraft properties during TWP-ICE, *J. Geophys. Res.*, 114, D04206, doi:10.1029/2008JD010851.
- Xie, S., et al. (2002), Intercomparison and evaluation of cumulus parameterizations under summertime midlatitude continental conditions, *Q. J. R. Meteorol. Soc.*, 128(582), 1095–1135, doi:10.1256/003590002320373229.
- Xie, S., et al. (2005) Simulations of midlatitude frontal clouds by single-column and cloud-resolving models during the Atmospheric Radiation Measurement March 2000 cloud intensive operational period, *J. Geophys. Res.*, 110, D15S03, doi:10.1029/2004JD005119.
- Xie, S., T. Hume, C. Jakob, S. Klein, R. McCoy, and M. Zhang (2010), Observed large-scale structures and diabatic heating and drying profiles during TWP-ICE, *J. Clim.*, 23(1), 57–79, doi:10.1175/2009JCLI3071.1.
- Xu, K.-M., et al. (2002), An intercomparison of cloud-resolving models with the Atmospheric Radiation Measurement summer 1997 Intensive Observation Period data, *Q. J. R. Meteorol. Soc.*, 128(580), 593–624, doi:10.1256/003590002321042117.
- Zhang, G. J. (2009), Effects of entrainment on convective available potential energy and closure assumptions in convection parameterization, *J. Geophys. Res.*, 114, D07109, doi:10.1029/2008JD010976.
-
- A. S. Ackerman and A. M. Fridlind, NASA Goddard Institute for Space Studies, 2880 Broadway, New York, NY 10025, USA.
 J.-P. Chaboureau and J.-P. Pinty, Laboratoire d'Aérologie, Observatoire Midi-Pyrénées, 14, avenue Belin, F-31400 Toulouse, France.
 J. Fan and S. A. McFarlane, Department of Climate Physics, Pacific Northwest National Laboratory, Richland, WA 99352, USA.
 A. Hill and B. Shipway, Met Office, FitzRoy Road, Exeter EX1 3PB, UK.
 A. Varble and E. J. Zipser, Department of Atmospheric Sciences, University of Utah, 135S 1460E, Rm. 806C, Salt Lake City, UT 84112-0110, USA. (a.varble@utah.edu)